



UNIVERSITÀ
DEGLI STUDI
DI PADOVA

Fuel Moisture Monitoring in Mediterranean Forests Using Sentinel-1 Imagery

by

Adedipe, Opeyemi Emmanuel

Previous Degrees (B.Agric.Tech. Crop, Soil and Pest Management, Federal University of
Technology, Akure, 2018)

A Report Submitted in Partial Fulfillment of the Requirement for the
Degree of:

Master of Forestry, University of New Brunswick
and

Master of Science in Forest Science, University of Padova

Supervisors:

Brigitte Leblon, Ph.D., Forestry and Environmental Management
Francesco Pirotti, Ph.D., Forestry and Agro-Environmental Sciences
Jasen Golding, MFE, RPF, Forestry and Environmental Management

This report is accepted by the
Dean of Graduate Studies

THE UNIVERSITY OF NEW BRUNSWICK

February 2023

©Adedipe, Opeyemi Emmanuel, 2023

Abstract

In fire-prone Mediterranean regions, fire danger is monitored using the Canadian Forest Fire Danger Rating system. The system's Fire Weather Index moisture codes are interpolated from single-point weather data. An alternative is to use remote sensing imagery that can provide spatially-explicit data at a repetitive time. The current study investigates the capability of multi-temporal Sentinel-1 C-band imagery to map Drought Code values for a study area of 502.42 km² in North-western Portugal. Backscatter values from 276 Sentinel-1 C-VV and C-VH images acquired between January 2018 and December 2020 were compared with five Drought Code classes in unburned and burned sites. The Drought Code values used in the study were estimated with the JRC's High-Resolution model. In addition, confounding variables such as tree cover, and incidence angle were considered. Our results show that: a) C-VV and C-VH backscatter correlate significantly ($p < 0.001$) with the Local Incidence Angle with $R^2 = 0.324$ to 0.438 , and the highest coefficients of determination occurred for the wet soils (DC class = 0 to 1), b) C-VV and C-VH backscatters can discriminate wet to dry forest environments, but they are less sensitive to the transition between dry (DC classes=1 to 10, 10 to 100) and extremely dry environments (DC classes=100 to 1000), c) the C-VH backscatter has a higher degree of prediction between the Drought Code classes in the unburnt, pre-fire and post-fire areas than the C-VV backscatter, d) the C-VH polarization captures post-fire recovery after an average minimum period of 360 days after the fire event, although with less distinction for extremely wet soils e) Mean backscatter values decrease with DC classes in unburnt, pre-

fire and post-fire (after 360 days) areas. Further studies are, however, required using high-resolution DC values in other Mediterranean regions that contain other tree species.

Acknowledgements

I sincerely appreciate the supervisors of this research work in the persons of Professor Brigitte Leblon, Professor Francesco Pirotti, and Mister Jasen Golding for the numerous support and valuable guidance provided. Special thanks to Doctor San-Miguel-Ayaz Jesus of the EU Joint Research Center for providing spatially-derived DC datasets. Also, I want to profoundly appreciate laboratory members, family, and friends for the invaluable support and encouragement received during this engagement.

Table of Contents

Abstract	ii
Acknowledgements	iv
Table of Contents	v
List of Tables.....	vii
List of Figures	viii
List of Abbreviations	x
1. Introduction	1
2. Literature Review	4
2.1 Background on Canadian Forest Fire Danger Rating System.....	4
2.2 Background on Synthetic Aperture Radar in fire studies.....	5
3. Materials and Methods.....	6
3.1 Study Area	6
3.2 SAR Imagery	7
3.3 Fire Maps.....	9
3.4 Tree Cover Map	9
3.5 Drought Code Map	11
3.6 Data Processing.....	14
3.6.1 Local Incidence Angle Masking	15
3.6.2 Tree Cover Masking.....	17
3.6.3 Forest Loss Masking	18
3.6.4 Final Synthetic Aperture Radar (SAR) Mask.....	19
3.6.5 Backscatter Values Extraction	20
4. Results and Discussion	22
4.1 Unburnt Areas.....	22

Linear Regression Parameters	24
4.2 Burnt Areas.....	29
5. Conclusions	35
References	36
Appendix: Regression Equation.....	44
Curriculum Vitae	

List of Tables

Table 1: Characteristics of the selected scenes with corresponding interpolated mean Drought Code (DC) values.	8
Table 2: Linear regression between C-VH backscatter values of unburnt pixels and LIA as a function of the sensor, polarization, and DC class. All the regressions are significant at $p < 0.001$. The Colors of the DC-Class column reflect the colours in plots of (Figure 16).....	24

List of Figures

Figure 1: Structure of the Canadian Forest Fire Rating System (adapted from [5]).	1
Figure 2: Structure of the Canadian Forest Fire Weather Index (adapted from [4]).	2
Figure 3: Location of the study area and corresponding digital elevation model (DEM).	7
Figure 4: Location of the fires in the area that occurred in 2018, 2019, and 2020.	9
Figure 5: Distribution of the tree cover (%) in the area obtained from Hansen et al. (2013)'s tree cover map.	11
Figure 6: Drought Code values distribution for each month in 2018.	12
Figure 7: Drought Code values distribution for each month in 2019.	13
Figure 8: Drought Code values distribution for each month in 2020.	13
Figure 9: Flowchart describing the methodology used in the study.	15
Figure 10: Local Incidence Angle (LIA) map of the study area extracted from Google Earth.	16
Figure 11: Local Incidence Angle (LIA) mask created from the LIA map.	17
Figure 12: Tree cover mask created from the tree cover distribution map.	18
Figure 13: Resulting mask obtained by overlaying the masks for tree cover, tree loss, and Local Incidence Angle (LIA). "Processed" pixels are characterized by a) tree cover higher than 90%, b) a Local Incidence Angle (LIA) lower than 65°, and c) a tree loss of 0%.	20
Figure 14: Example of a C-VV SAR image overlaid with Figure 3.1.1 mask. The pixels displayed in grey correspond to "unprocessed" pixels in (Figure 13).	20
Figure 15: 500 m buffer geometry from DC pixel centers overlapping the masked SAR data. SAR backscatter values were correlated to DC values at the time of the image.	21
Figure 16: Linear regression relationship between uncorrected backscatter values and LIA in unburnt pixels as a function of the DC class, for (a) Sentinel-1A (C-VH); (b) Sentinel-1A (C-VV); (c) Sentinel-1B (C-VH); (d) Sentinel-1B (C-VV). The regression parameters are presented in (Table 4.1).	23

Figure 17: Relationship between the LIA and corrected backscatter values in unburnt pixels with the DC classes, for (a) Sentinel-1A (C-VH); (b) Sentinel-1A (C-VV); (c) Sentinel-1B (C-VH); (d) Sentinel-1B (C-VV).....26

Figure 18: Distribution of corrected backscatter values in unburnt pixels with the DC classes, for (a) Sentinel-1A (C-VH); (b) Sentinel-1A (C-VV); (c) Sentinel-1B (C-VH); (d) Sentinel-1B (C-VV).....28

Figure 19: Distribution of corrected backscatter values before fire in fire-affected pixels with the DC classes, for (a) Sentinel-1A (C-VH); (b) Sentinel-1A (C-VV); (c) Sentinel-1B (C-VH); (d) Sentinel-1B (C-VV).30

Figure 20: Distribution of corrected Sentinel-1A C-VH backscatter, grouped by DC class for (a) 0 to 30; (b) 30 to 90; (c) 90 to 180; (d) 180 to 360; (e) 360 to inf days after the fire event.....32

Figure 21: Distribution of corrected Sentinel-1B C-VH backscatter, grouped by DC class for (a) 0 to 30; (b) 30 to 90; (c) 90 to 180; (d) 180 to 360; (e) 360 to inf days after the fire event.....33

List of Abbreviations

ASL	Above Sea Level (m)
BUI	Build Up Index
CCFDRS	Canadian Forest Fire Danger Rating System
DC	Drought Code
DEM	Digital Elevation Model (m)
DMC	Duff Moisture Code
DTM	Digital Terrain Model (m)
FFMC	Fine Fuel Moisture Code
FWI	Fire Weather Index
GRD	Ground Range Detected
HRES	High Resolution
ISI	Initial Spread Index
IW	Interferometric Wide
LIA	Local Incidence Angle (°)
NWP	Numerical Weather Prediction
SAR	Synthetic Aperture Radar
TOPSAR	Terrain Observation with a Progressive Scanning

1. Introduction

Forest fires are an essential disturbance affecting forest ecosystem dynamics in several forested ecosystems, particularly in the Mediterranean regions. Mediterranean Europe has been highly susceptible to mega-fires due to drought and topography that promote fire ignition [1][2]. Italy, France, and Spain have consequently been identified with numerous fire events, with more than 100,000 ha annually burned [3].

In the Mediterranean region, fire danger is monitored using the Canadian Forest Fire Danger Rating System (CFFDRS) (Figure 1). One of its systems is the Fire Weather Index (FWI), comprising fuel moisture codes and fire behaviour sub-indexes (Figure 2). The system estimates mid-afternoon fire danger based on weather variables (temperature, wind speed, and relative humidity) observed at noon and rainfall intensity measured in 24 hours[4].

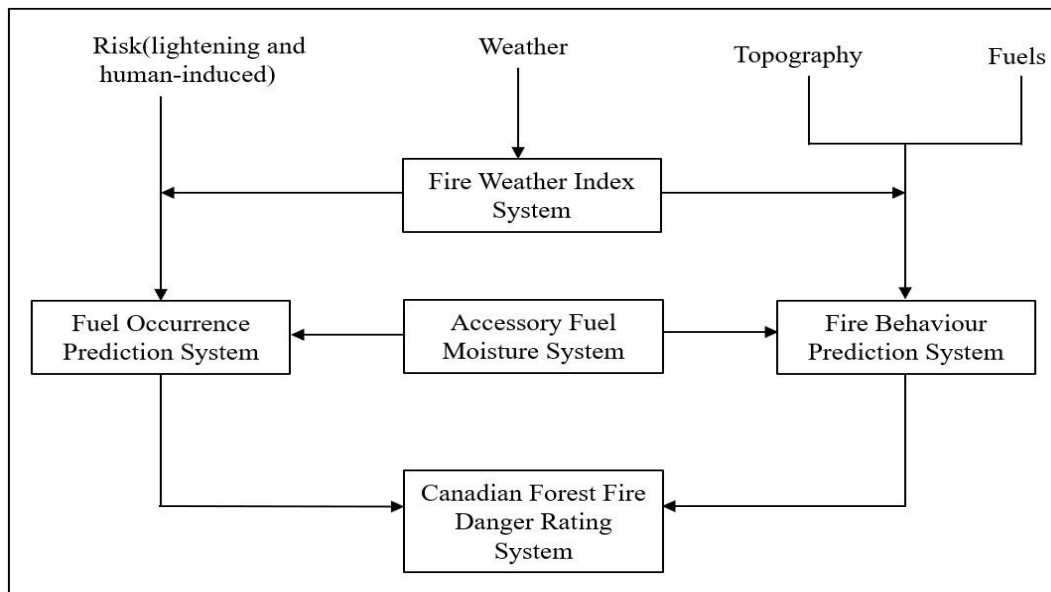


Figure 1: Structure of the Canadian Forest Fire Rating System (adapted from [5]).

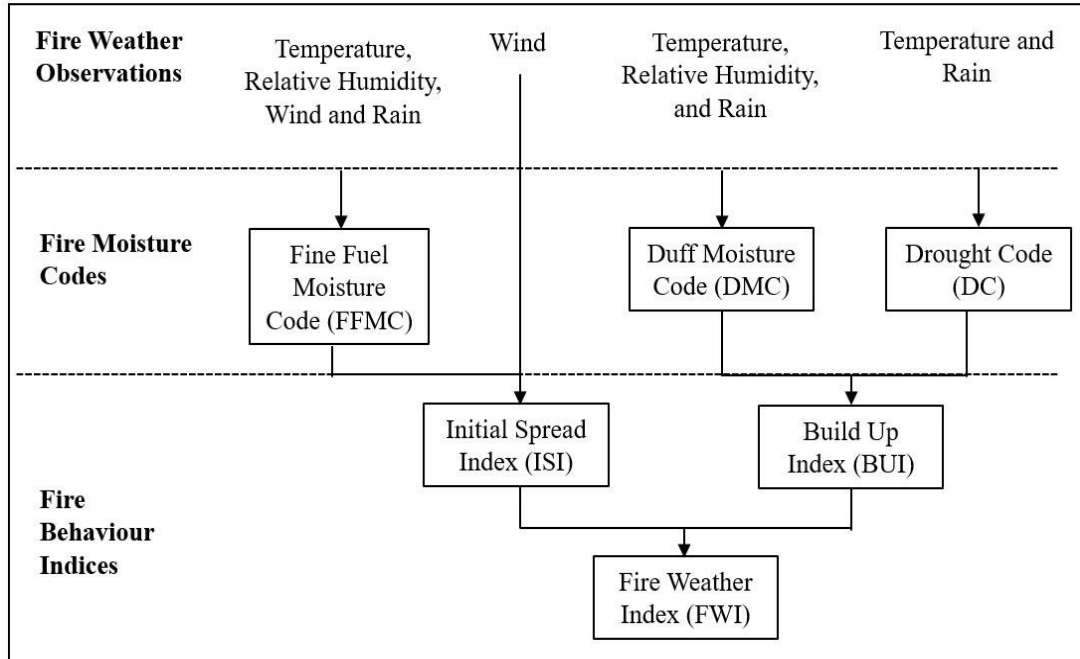


Figure 2: Structure of the Canadian Forest Fire Weather Index (adapted from [4]).

However, the predictability of fire danger with FWI is limited to small geographical areas, mainly when meteorological observations are collected at sparse weather stations [6]. For the Mediterranean regions, the EU Joint Research Center (JRC) uses Numerical Weather Prediction (NWP) and High Resolution (HRES) models for interpolating between the weather station data. As shown in [7], the HRES model operates at a horizontal resolution of 16 km and provides accurate weather prediction for ten days upfront. Another limitation of FWI is its standard configuration for only two pine species [8], and thus cannot be readily applicable to other forest types.

A suitable alternative is to use remote sensing [9][10]. Among all the FWI codes, the Drought Code (DC) can be considered a reliable proxy in estimating fuel moisture. Strong correlations were found between DC and NOAA-AVHRR optical data in Indonesia [11]

and Canadian boreal forests [6]. However, optical imagery has the drawback of limited availability to clear sky conditions. This is not the case with active SAR sensors that can acquire images, whatever the sky conditions. Synthetic Aperture Radar (SAR) sensors provide fine spatial resolution data and allow for 24-hour image acquisition, even in meteorological situations perturbing optical satellites' efficacy [12][13].

The main objective of this study is to assess the capability of Sentinel-1 C-VV and C-VH radar backscatters in delineating moisture regimes, as defined by DC values in North-western Portugal. As a secondary objective, differences in the sensitivity of C-VV and C-VH backscatters for mapping pre-fire and post-fire moisture conditions will also be assessed. Both variables (backscatter and DC) were acquired from the 2018 – 2020 time series. The analysis will be done only for sites with substantial tree cover to reduce the tree cover's effects. In the study, we will also consider the effect of the local incidence angle on the radar backscatter. In particular, the analysis will be performed in three types of areas: a) unburnt areas, b) burnt areas before the fire (pre-fire), and c) burnt areas after the fire (post-fire). The relationship between backscatter values and DC classes as a function of the Local Incidence Angle (LIA) will be investigated with linear regression models. Corrected backscatter values will be analyzed with box plots as a function of DC classes, satellite and polarization.

2. Literature Review

2.1 Background on Canadian Forest Fire Danger Rating System

Several factors have been linked to forest fire incidences in the European Mediterranean region, which include land surface temperature, terrain morphology, canopy closure, and fuel moisture distribution [14][15]. In the European Mediterranean region, fire danger is monitored using the CFFDRS. It is a numerical forest rating system that uses daily weather data to predict the probability of fire ignition, fire control complexity, and fire spread easiness [16]. One of the CFFDRS systems is the Fire Weather Index system. It has several fuel moisture codes. According to [8], the Fine Fuel Moisture Code (FFMC) is related to pine litter of 1.2 cm thickness and fuel weight of 0.25 kg/m². The Duff Moisture Code (DMC) is the moisture of the top 7 cm of forest layers where decay occurs with a fuel load of 5 kg/m². The (DC) is the moisture availability at 18 cm thickness of organic matter and fuel capacity of 25 kg/m². These three codes are related to a different fuel that has a time-lag period or the time elapsed for two-thirds loss of soil moisture at 20°C and 40% RH [4][17]. FFMC has a time lag of 2/3 day, DMC has a time lag of 12 days, and DC has a time lag of 52 days.

Furthermore, the drying rate of each fuel type significantly depends on the previous day's code values [4]. Fuel behaviour indices include Initial Spread Index (ISI), Buildup Index (BUI), and the Fire Weather Index (FWI). The CFFDRS was developed over data acquired over mature jack pine (*Pinus banksiana*) and lodge pole pine (*Pinus contorta*) forests, with the hypothesis that these two pine species have similar structural arrangements and fire dynamics as all other forests [8]. The CFFDRS FWI codes have been tested abroad. Yang

& Di [18] evaluated the applicability of the CFFDRS to monitor fire dangers in North-Eastern China, where climatic conditions are similar to Canadian boreal forests. Strong correlations were also derived between the DC and the number of fire occurrences in a *Pinus halepensis* forest in the Greek Mediterranean region, where the forest types differ from the Canadian boreal forests [19].

2.2 Background on Synthetic Aperture Radar in fire studies

Radar imageries were shown to be very suitable in several fire studies. Cross-polarized (C-VH) backscatter is excellent for assessing the difference between bare land and forests, while the C-HH co-polarization is best for detecting the backscatter sensitivity to soil moisture after fire incidents [13][20]. DC values were shown to correlate well with SAR C-band backscatter extracted from RADARSAT-1 and ERS (1 and 2) imagery in northern boreal forests [17][21][22] and RADARSAT-2 polarimetric data [20]. However, according to [23], SAR beams are also sensitive to terrain roughness and biomass build-up.

Among all the new SAR sensors, Sentinel-1 has several advantages. It is a constellation system, i.e., two orbiting platforms (Sentinel-1A and -1B) that allow image acquisition at 10 m resolution with a 6-day repeat cycle in horizontal and vertical polarization modes (VV and VH) [24]. Sentinel-1 C-VV and C-VH backscatter variations were linked to meteorological events, forest floor moisture, and canopy moisture in a deciduous forest in France [25]. Sentinel-1 C-VV imagery was used to estimate soil moisture in open sites in India [26] and over a mixed forest in the United States [27].

The study aims to assess the capability of Sentinel-1 C-VV and C-VH backscatters to assess wet/dry soil conditions that are defined based on DC values in the case of a

Mediterranean region of Northern Portugal. Since the CFFDRS-derived DC does not consider the spatial heterogeneities between sites, it is a good surrogate for proxying soil moisture variation, which can explain why sites might be prone to fire occurrences. In addition, confounding variables, i.e., local incidence angle and tree cover, will also be considered in the analysis.

3. Materials and Methods

3.1 Study Area

The study area of 502.42 km² is located in the municipalities of Viana do Castelo and Braga in North-western Portugal (41- 42° North Latitude, 8 - 9° West Longitude) (Figure 3). The area elevation ranges from 0 m above sea level (ASL) in the vicinity of Viana do Castelo and Braga to 1500 m ASL at the bordering regions of Melgaço and Cabeceiras de Basto (Figure 3). From the vegetation point of view, the study area includes broadleaf and conifer tree species, mainly the maritime pine (*Pinus pinaster*) and eucalyptus (*Eucalyptus globulus*) [28]. According to the Köppen-Geiger climate classification [29], both municipalities are classified as CSB, meaning a warm temperate climate with dry and warm summers. Between 1981 and 2010, the mean daily temperatures were the highest in August in Viana do Castelo (20.8°C) and Braga (21.4°C) [30]. Over the same period, the mean precipitations were 38.5mm (Viana do Castelo) and 21.4mm (Braga). Such climatic conditions are related to high land surface dryness and, thus, the susceptibility to fire incidences [31]. The EU Joint Research Centre (JRC) reported that 70% of fire incidents

in 2020 in Portugal occurred in July, August, and September [32]. In 2006, fire events affected 15,706 ha in Viana do Castelo and 10,265 ha in Braga [33].

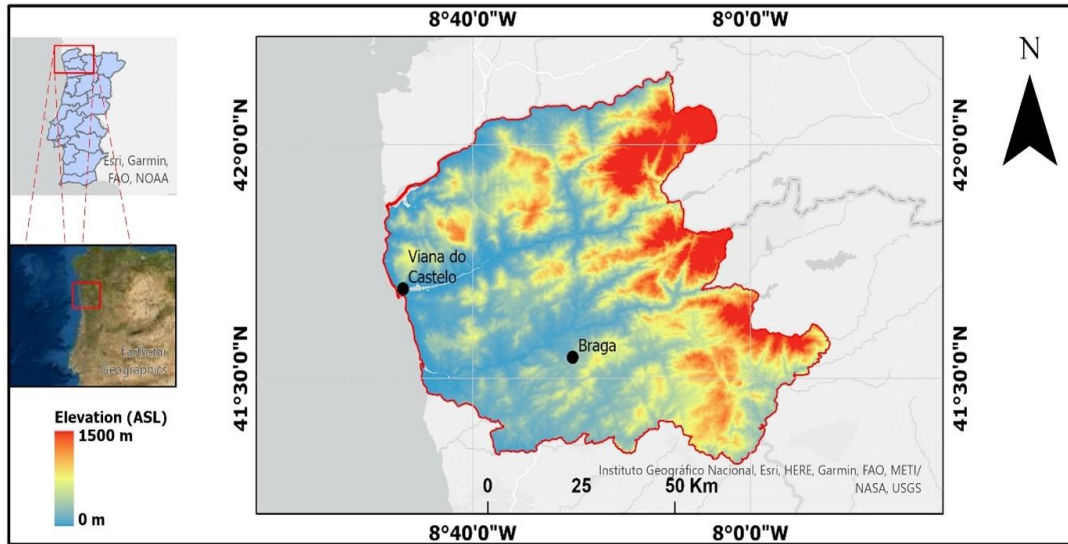


Figure 3: Location of the study area and corresponding digital elevation model (DEM).

3.2 SAR Imagery

This study used SAR imagery acquired by the European Space Agency (ESA) Sentinel-1 (S1) satellite, having the TOPSAR (Terrain Observation with a Progressive Scanning SAR) sensor. Sentinel-1 consists of a constellation of two satellites, A and B, each having a sensor that operates in the C-band with a central frequency of 5.405 GHz and a wavelength of 5.6 cm [24]. The first Sentinel-1 platform was launched in April 2016. With a swath width of 250 km, it provides a return time of about six days. A total of 276 scenes covering the study area were downloaded from Scihub Copernicus Hub (<https://scihub.copernicus.eu/>), covering 181 days over the three years (2018, 2019, and 2020) that are considered in this study. The image data consisted of Level-1 Ground Range Detected (GRD) types in the high-resolution Interferometric Wide (IW) swath mode. The scenes were from the same ascending orbit (147), thus having the same incidence angles between 30.42 and 46.03°

from one date to another. Furthermore, local incidence angles ranging from 2.07 to 64.72° were constant from one date to another, as the area's topography does not change with time.

Table 1: Characteristics of the selected scenes with corresponding interpolated mean Drought Code (DC) values.

Year	Date	Orbit	ID	Mean DC
2018	21/01	59	68110	11.79
	26/02	62	72497	19.2
	22/03	64	75497	5.83
	27/04	67	79818	58.96
	21/05	69	82178	139.97
	14/06	71	85552	53.82
	20/07	74	89703	206.84
	13/08	76	92438	394.85
	18/09	79	96580	607.43
	24/10	82	100702	352.86
	17/11	84	103515	15.96
	23/12	87	107882	4.36
2019	28/01	90	112232	10.05
	21/02	92	115173	7.22
	29/03	95	119565	53.13
	22/04	97	122536	19.23
	28/05	100	126820	99.13
	21/06	102	129488	133.35
	27/07	105	133436	323.56
	20/08	107	136188	281.57
	25/09	110	140359	277.76
	31/10	113	145549	5.82
	24/11	115	147435	2.77
	30/12	118	151709	1.98
2020	23/01	120	154561	5.74
	16/02	122	157453	7.20
	23/03	125	161731	10.81
	16/04	127	164568	3.50
	22/05	130	168700	58.45
	15/06	132	171392	138.96
	21/07	135	175485	356.82
	14/08	137	178225	479.65
	19/09	140	182437	456.48
	25/10	143	186640	25.43

18/11	145	189433	5.78
24/12	148	193752	2.23

3.3 Fire Maps

Because the study aims to analyze the dynamics of the relationship between the DC and backscatter before and after fire events, we used fire maps in the analysis. They were extracted from the European Forest Fire Information System (EFFIS) (<https://effis.jrc.ec.europa.eu>) [34]. The maps provide the occurrence of fire activities over the three years study period (Figure 4). They show that fire areas range from 2 ha to 675 ha. Vegetation in these fire-affected areas includes broad leaves and conifers.

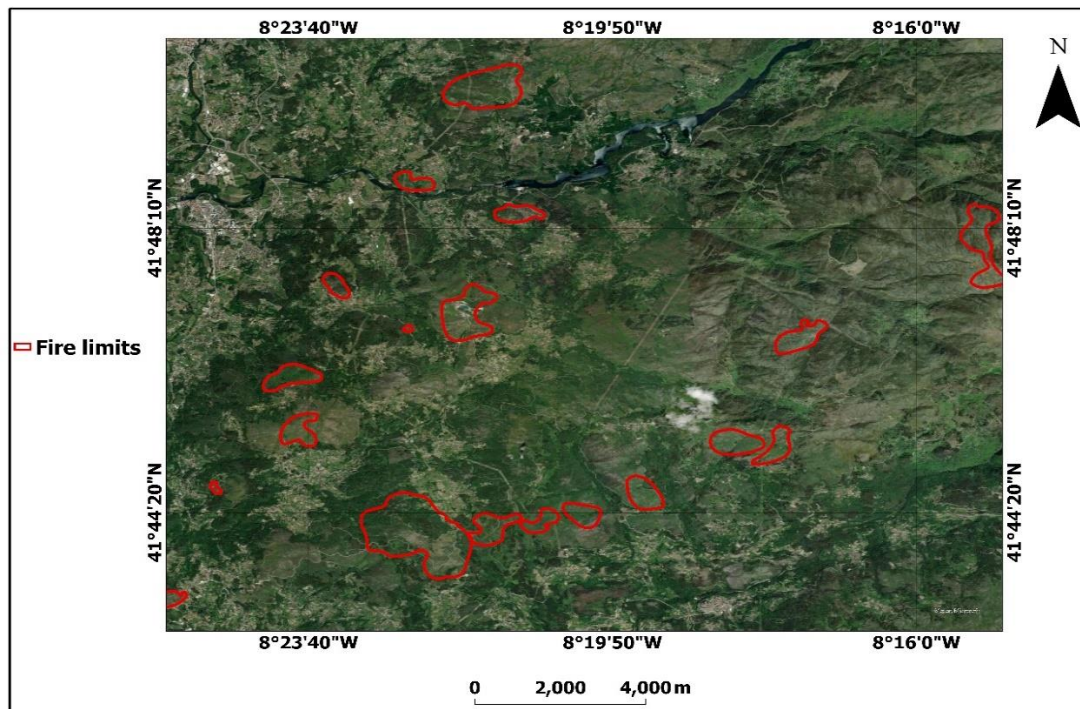


Figure 4: Location of the fires in the area that occurred in 2018, 2019, and 2020.

3.4 Tree Cover Map

As shown in [21], the relationship between SAR backscatters and DC values highly depends on the tree cover. In particular, the relationship between SAR backscatters and DC

values differs for burned and unburned areas. Also, recovery mechanisms from fires in Mediterranean forests depend on the tree cover [35][36]. Therefore, the study only considered unburnt and burnt (pre-fire periods) sites with substantial tree cover. To define such sites, we used tree cover data that were extracted from the tree cover map of [36] and retrieved from the Global Forest Change website (<https://glad.earthengine.app/view/global-forest-change>) (Figure 5). The map provides the global tree cover from 2000 to 2020, with values from 0% (no forest) to 100 % (full tree cover). The map has a resolution of 30 m because it was produced by classifying Landsat images. The information from [36] also allowed to map the areas with forest loss due to disturbances. For example, Portugal lost a cumulative of 1.03 million ha from 2001 to 2019 of Mediterranean forests [37].

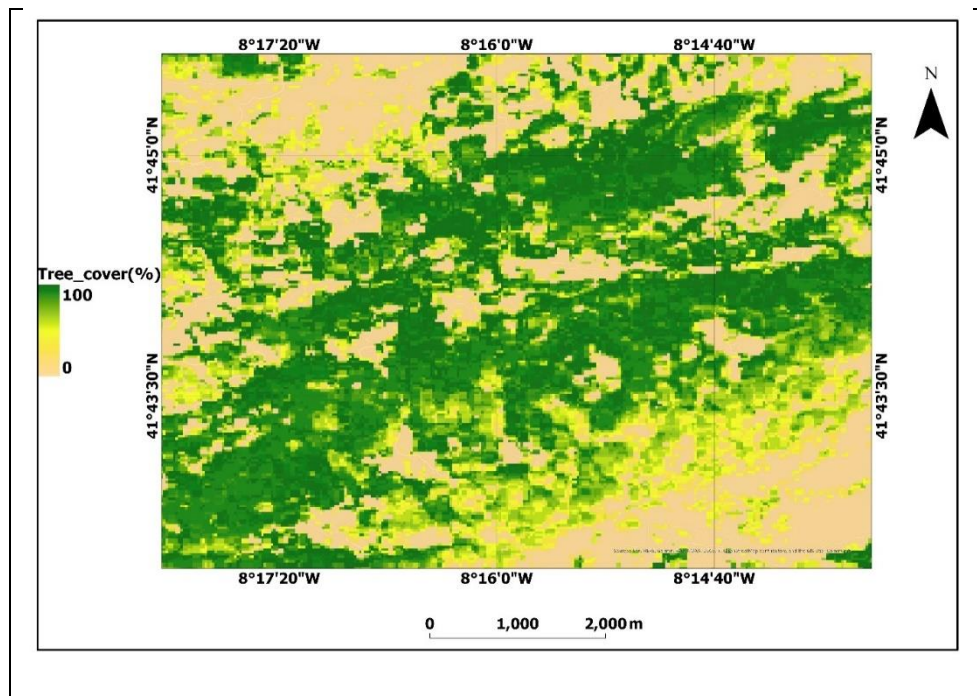


Figure 5: Distribution of the tree cover (%) in the area obtained from Hansen et al. (2013)'s tree cover map.

3.5 Drought Code Map

Drought Code maps of the study area from 2018 to 2020 were obtained from JRC [38]. They are produced by interpolating DC values from the European Centre for Medium-Range Weather Forecast (ECMWF) network. The pixel resolutions of these maps are approximately 0.07° (~7 km at the average latitude of the study area) for 2019 and 2020 and 0.14° (~14 km at the average latitude of the study area) for 2018. According to [4] and [39], DC is calculated from daily temperature and precipitation records. For rainfall above 2.8 mm, DC is calculated based on rainfall values of the day (DC_r) and the DC value of the previous day (DC_{t-1}) with the following equations:

$$DC_r = 400 \cdot \ln\left(\frac{800}{Q_r}\right) \quad (1)$$

$$Q_r = Q_{t-1} + 3.937 \cdot r_d \quad (2)$$

$$Q_{t-1} = 800 \cdot \exp\left(\frac{-DC(t-1)}{400}\right); \quad r_d = 0.83 \cdot r_t - 1.27 \quad (3)$$

Where: DC_r is the drought code from rainfall data of the day, Q_r is the moisture equivalent that is calculated from the moisture equivalent of the previous day, Q_{t-1} , which is in turn calculated from DC_{t-1} , i.e., the DC code of the last day, r_t is rainfall of the day in mm.

In case of rainfall below 2.8 mm, DC is calculated based on the temperature at mid-day and DC_{t-1} , i.e., the DC code of the previous day with the following equations:

$$DC_t = DC_{t-1} + 0.5 \cdot V \quad (4)$$

$$V = 0.36 (T_{12} + 2.8) + Lf \quad (5)$$

Where V is the potential evaporation, T_{12} is the temperature at mid-day, and Lf is the seasonal day length adjustment.

Because the fire areas are much smaller than the DC map resolution, each DC value results from a bilinear interpolation weighted with distance from the center of the four DC cells. The resulting unitless DC values were classified as extremely low for values less than 256.1 and remarkably high for values greater than 749.4 [40]. Figures 6, 7, and 8 present the DC values distribution for each month in 2018, 2019, and 2020, respectively.

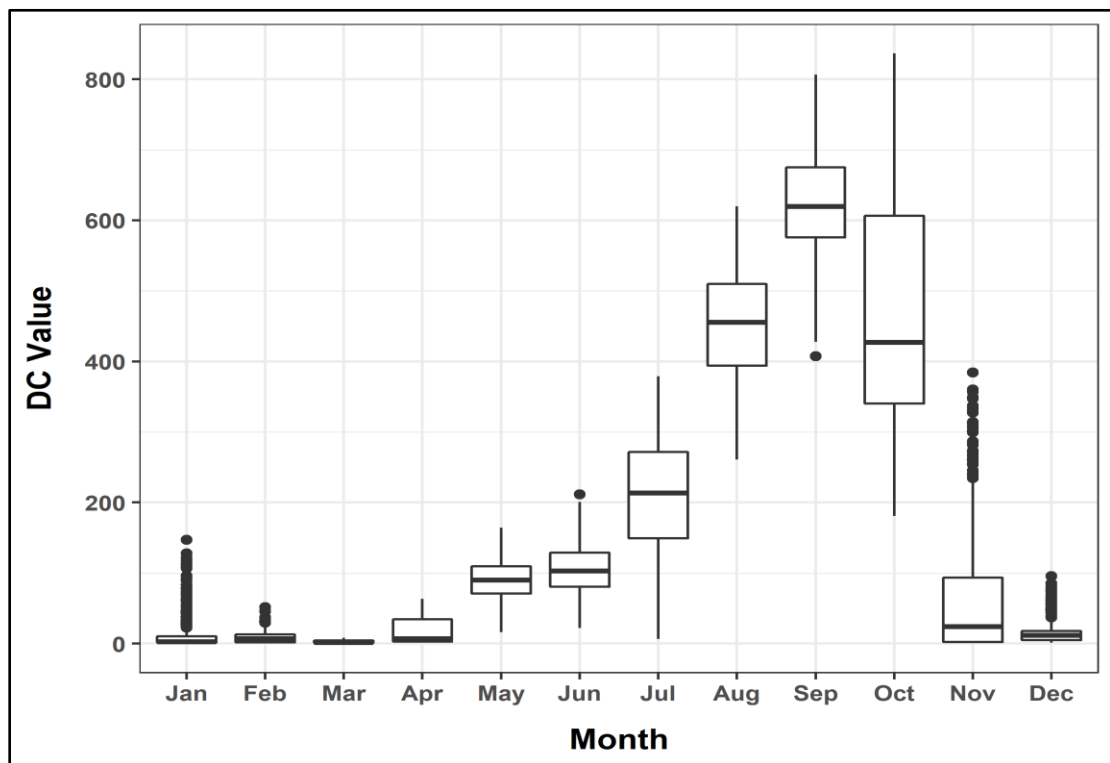


Figure 6: Drought Code values distribution for each month in 2018.

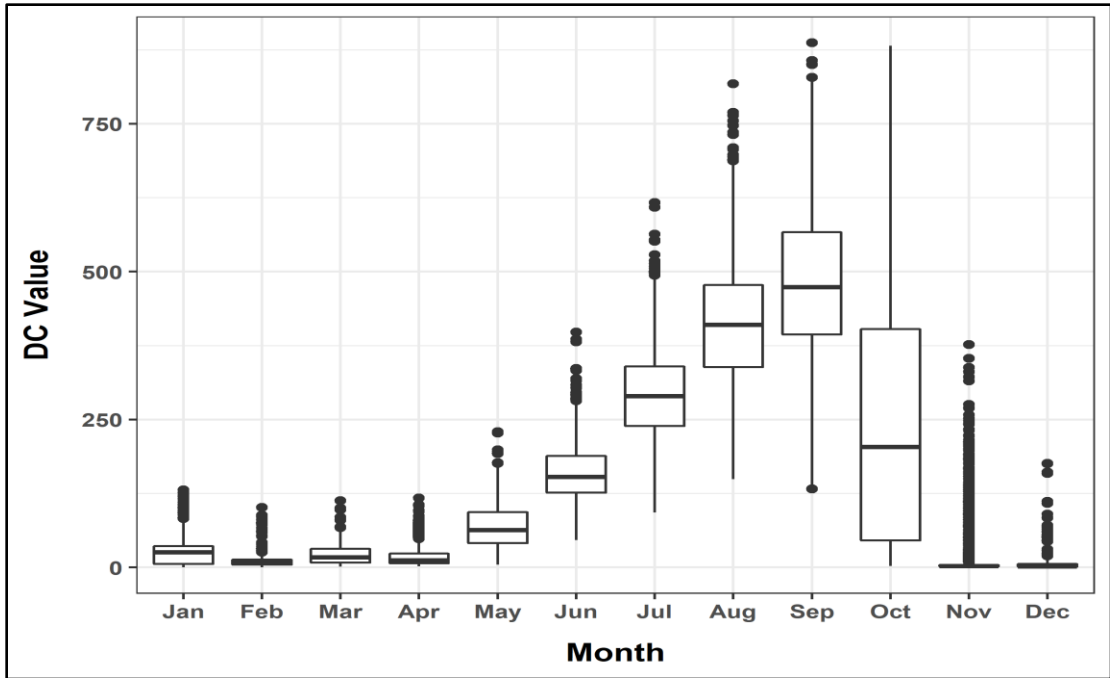


Figure 7: Drought Code values distribution for each month in 2019.

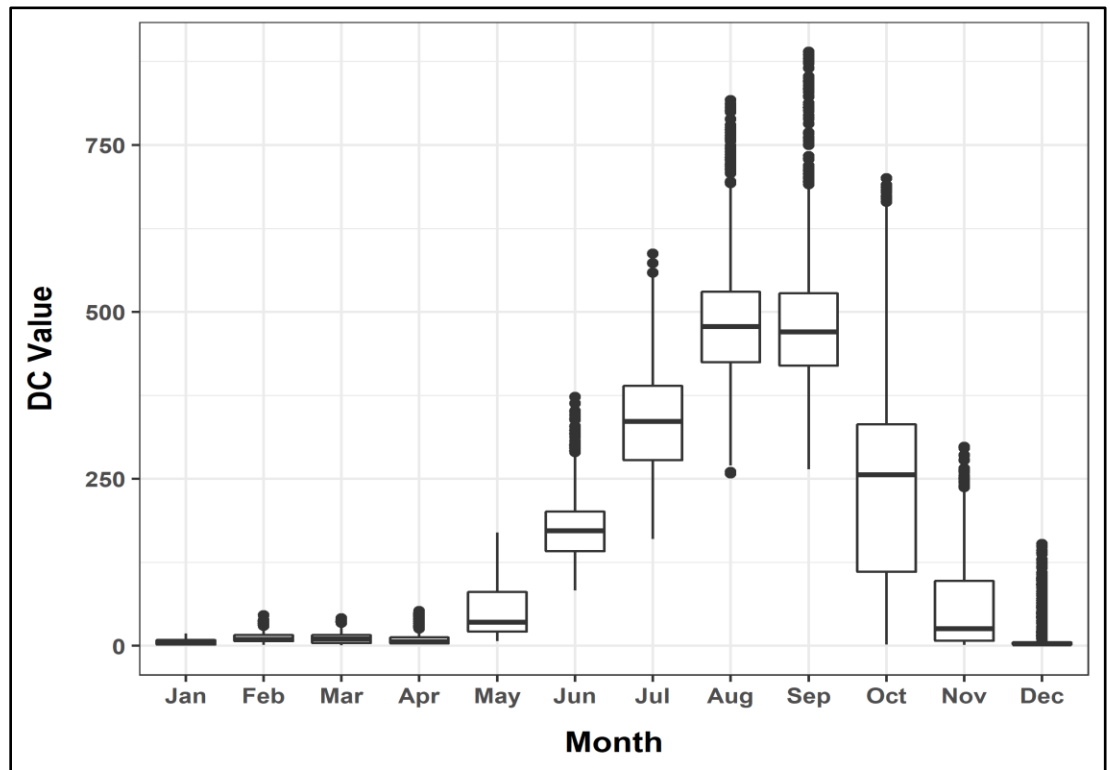


Figure 8: Drought Code values distribution for each month in 2020.

3.6 Data Processing

Figure 9 presents the methodology used in the study. Dual-polarized images acquired in the satellite's ascending orbit were processed in the Sentinel Application Platform (SNAP) to produce backscatter images (σ° in decibels (dB)). σ° represents the illuminated target's target backscattering area (radar cross-section). The SNAP platforms used the following steps: subsetting, precise orbit file correction, thermal noise removal, radiometric calibration, terrain correction, and conversion to dB. Multi-looking and speckle filtering were skipped to ensure detail preservation and no repetition of the multi-looking process usually done by the Sentinel-1 processing facility. The imagery was orthorectified to WGS 1984 coordinate system using the Shuttle Radar Topography Mission (SRTM) 3Sec Digital Elevation Model (DEM). The resulting SAR imagery was subjected to a series of masking as a function of the tree cover and local incidence angles to minimize the effects of these confounding variables.

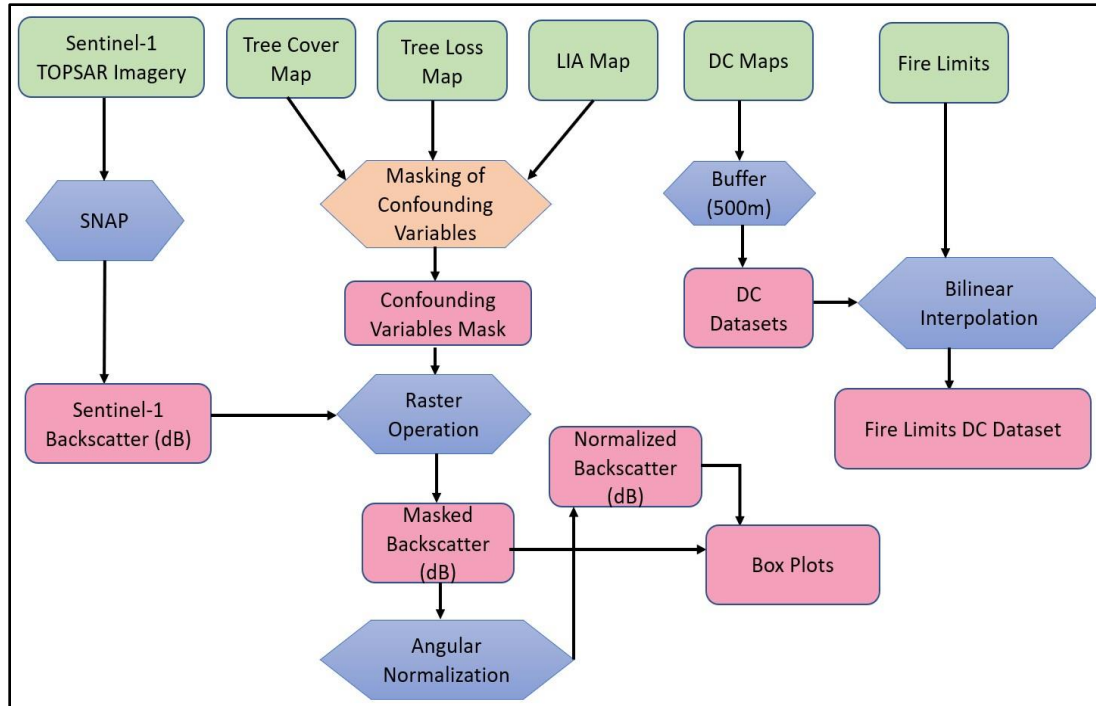


Figure 9: Flowchart describing the methodology used in the study.

3.6.1 Local Incidence Angle Masking

Local incidence angle (LIA) is defined as the angle of the incident radar beam to the normal of the local surface [41]. SAR backscatter is highly related to LIA [42]. In this study, we only considered the areas having an LIA of less than 65° . To do so, we created an LIA map using the data from the radar image geometry (look direction angle) and values of slope and aspect angle derived from a Digital Elevation Model (DEM) that provides elevation values of the earth's surface [43]. The resulting LIA map was cropped and resampled to match the radar imagery (Figure 10). Finally, it created an LIA mask that masks all the areas with LIA higher than 65° (Figure 11). As a result, the LIA value for each scene ranged from (2.07 to 64.72).

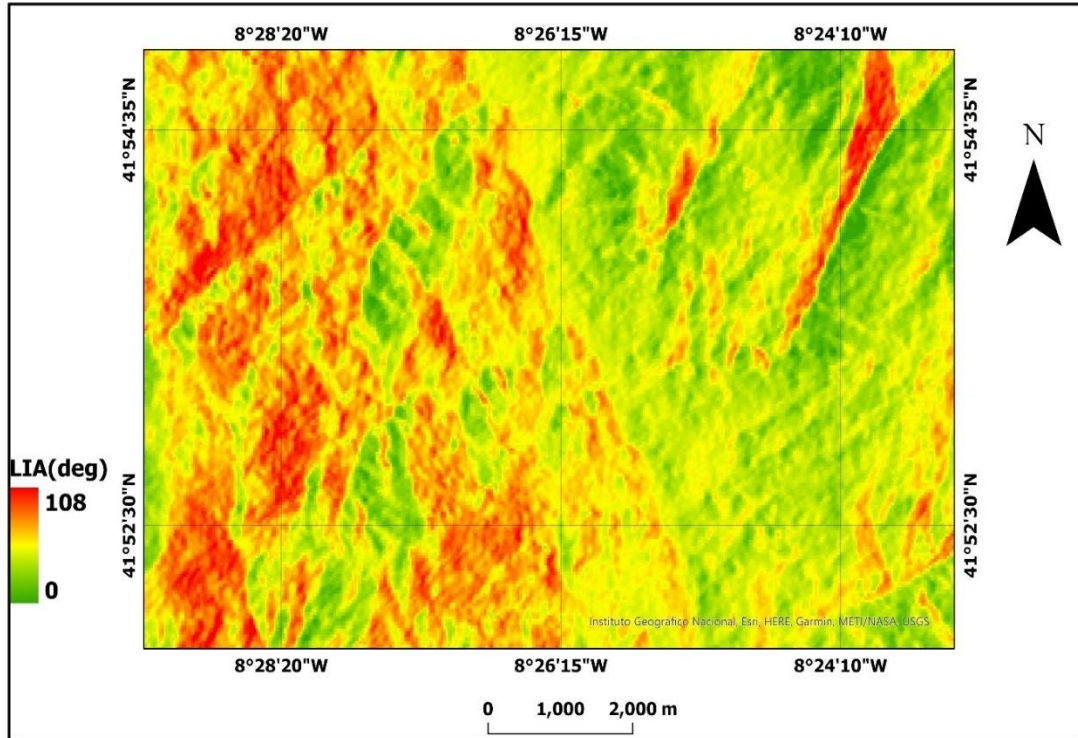


Figure 10: Local Incidence Angle (LIA) map of the study area extracted from Google Earth.

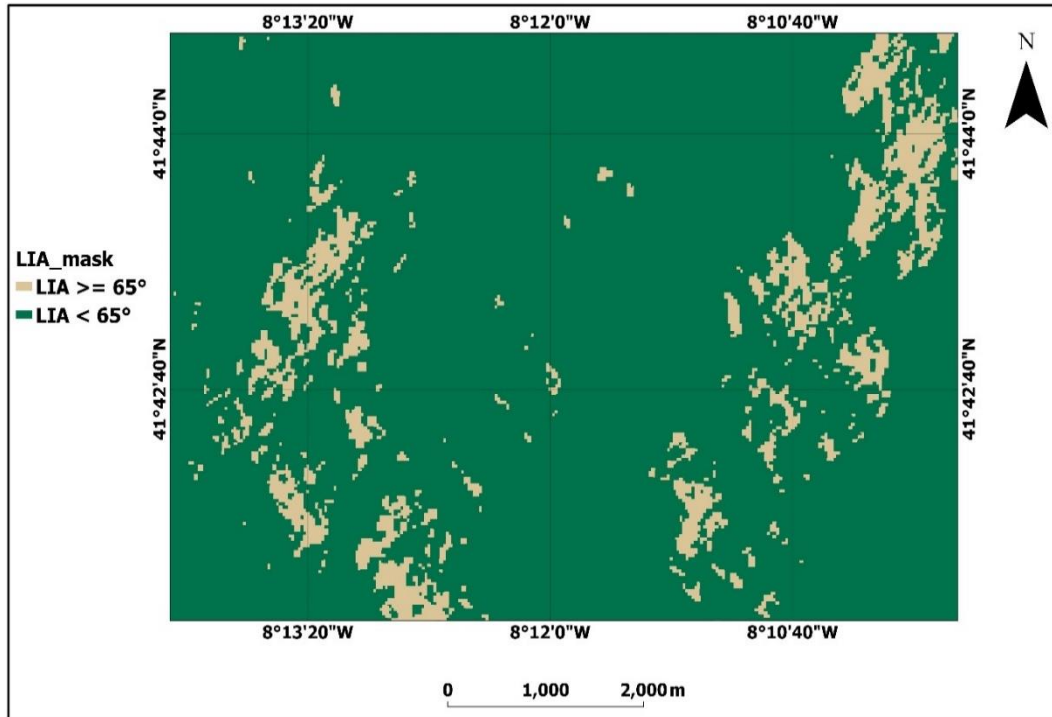


Figure 11: Local Incidence Angle (LIA) mask created from the LIA map.

3.6.2 Tree Cover Masking

For this research, only burnt (pre-fire periods) and unburnt areas with tree cover higher than 90% were considered, and the other regions were masked. Such a mask was created from the global scale tree cover of [36], a raster with global tree canopy cover percentage values for each pixel. Values range from zero (no canopy in the pixel) to 100 percent (pixels fully covered with forest canopy). The base map was created in 2000 and successively updated each year up to 2020 in terms of forest gain or loss.

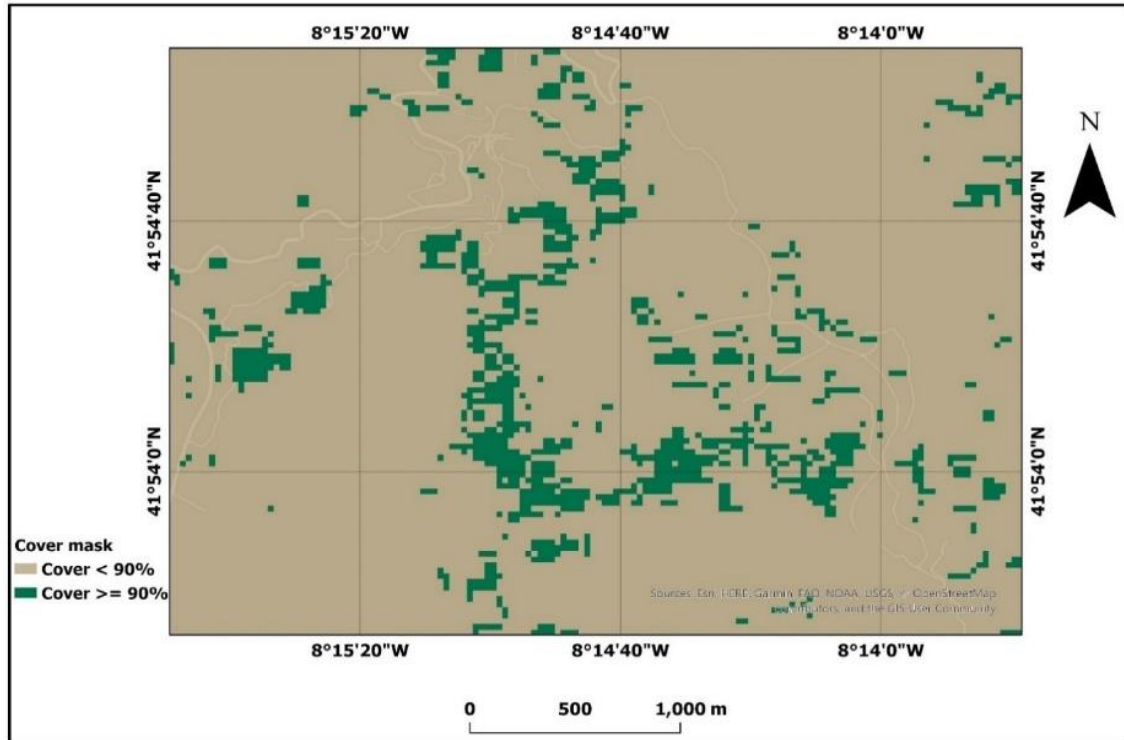


Figure 12: Tree cover mask created from the tree cover distribution map.

3.6.3 Forest Loss Masking

Forest cover loss occurs through different disturbances, including forest fires. Hansen et al. (2013)'s canopy cover map includes a loss and gain map. The former provides estimated global forest loss information from 2000 to 2020. Values in the map are integers from zero (no loss) to 20, with values above zero representing the loss year since 2000. Forest cover loss information was used to ensure that only areas without a loss (zero value at a pixel) or with loss due to fire were selected for further processing. The pixels with tree cover loss due to a fire event were defined as those with a loss value that spatially and temporally overlapped the fire polygons. These pixels were not masked as they were used in the analysis to assess backscatter behaviour changes before and after the fire event.

3.6.4 Final Synthetic Aperture Radar (SAR) Mask

A final mask was created by simple raster calculation that composited the three masks described above using a multiplication operation. The final mask allows keeping pixels with forest canopy cover above 90%, canopy loss equal to zero or only with fire loss, and LIA lower than 65°. The resulting pixels were defined as "processed" or "unprocessed" (Figure 13) for reference in the following steps. Backscatter values corresponding to "processed" pixels were further processed, while those corresponding to "unprocessed" pixels were not considered. Outlier backscatter values were removed by keeping only values below -0.1 and above -30 dB.

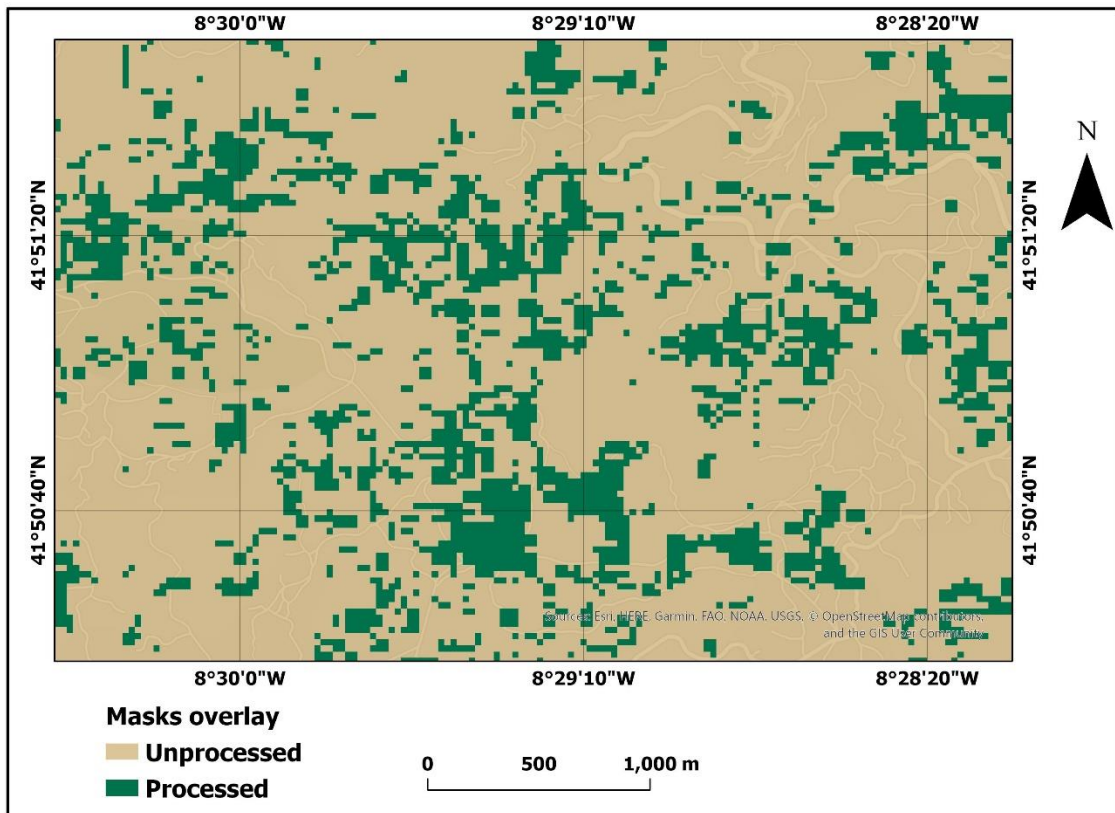


Figure 13: Resulting mask obtained by overlaying the masks for tree cover, tree loss, and Local Incidence Angle (LIA). "Processed" pixels are characterized by a) tree cover higher than 90%, b) a Local Incidence Angle (LIA) lower than 65° , and c) a tree loss of 0%.

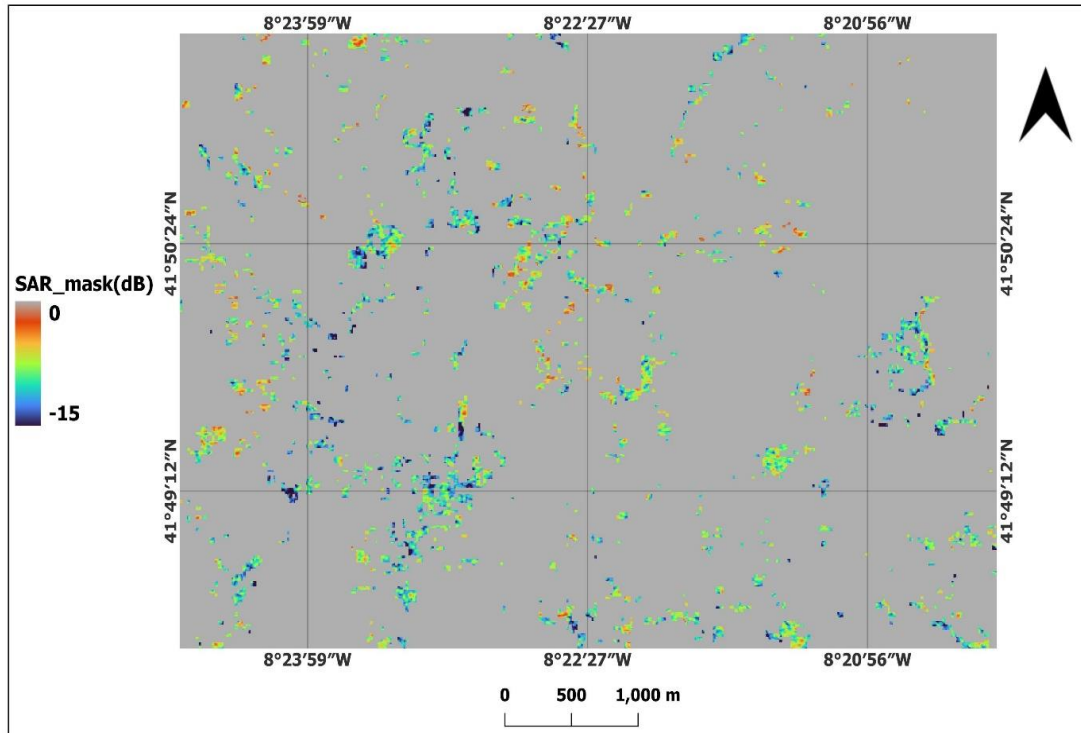


Figure 14: Example of a C-VV SAR image overlaid with Figure 3.1.1 mask. The pixels displayed in grey correspond to "unprocessed" pixels in (Figure 13).

3.6.5 Backscatter Values Extraction

Given that one of the study objectives is to analyze the relationship between radar backscatters and DC values, we used daily DC maps with a resolution of 0.14° in 2018 and 0.07° in 2019 and 2020. The study area corresponds to 60 cell centers for 2018 and 232 for 2019 and 2020. Cell centers of the DC rasters were buffered to a 500 m radius, and all Sentinel-1 pixels falling in the buffer were used to analyze the "Unburnt areas" dataset

(Figure 15). Finally, bilinear interpolation was used to assign DC values to SAR pixels in the fire polygons, as these maps are not centred on buffers of DC maps. This last step created the "Burnt areas Pre-Fire" and "Burnt Areas Post-Fire" datasets.

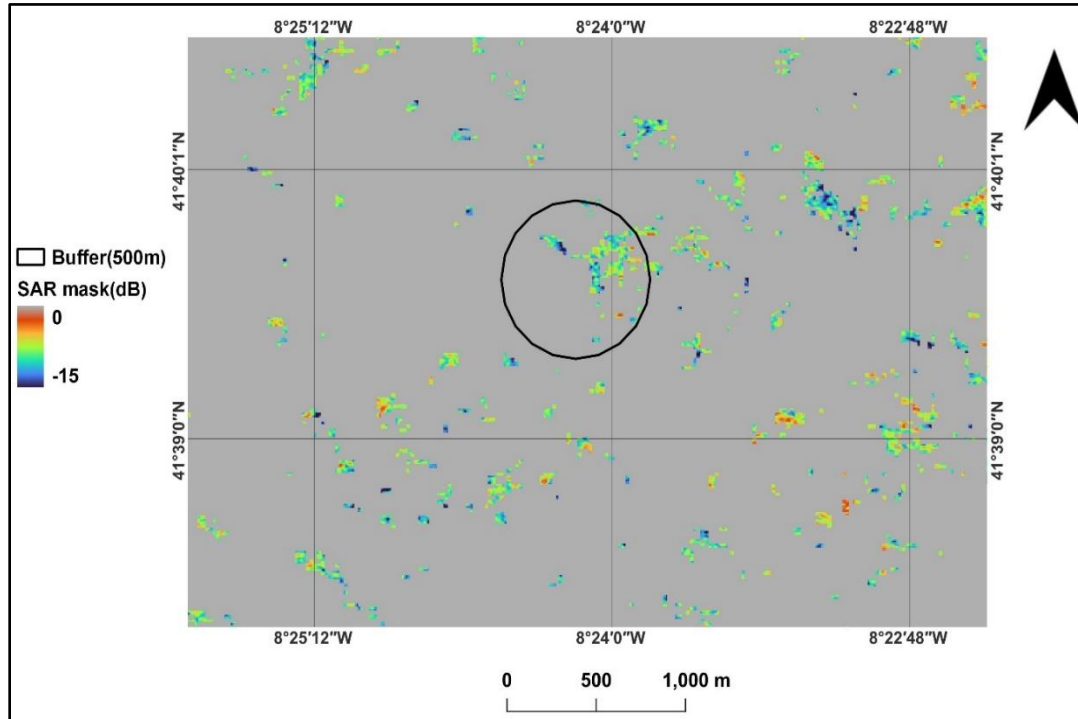


Figure 15: 500 m buffer geometry from DC pixel centers overlapping the masked SAR data. SAR backscatter values were correlated to DC values at the time of the image.

4. Results and Discussion

4.1 Unburnt Areas

Our first research question is how DC class affects the backscatter/LIA relation. Figure 16 presents the change of backscatter as a function of LIA values grouped by three factors: (i) the DC class, (ii) the polarization (VV or VH), and (iii) the Sentinel satellite (A or B). The DC values are divided in four classes using a log₁₀-scale (0.1-1, 1-10, 10-100, 100-1000). The log₁₀-scale was used to highlight the DC values of very wet canopy scenarios (0.1-1) from the dry and very dry scenarios. This choice is because the area has a dry Mediterranean climate. Thus, wet canopy scenarios are less frequent. The DC classes represent a transition between extremely wet and dry soil conditions in unburned areas. The figure shows that the backscatter decreases with LIA for this study's unburnt and burnt pixels. This result agrees with other studies [21][44].

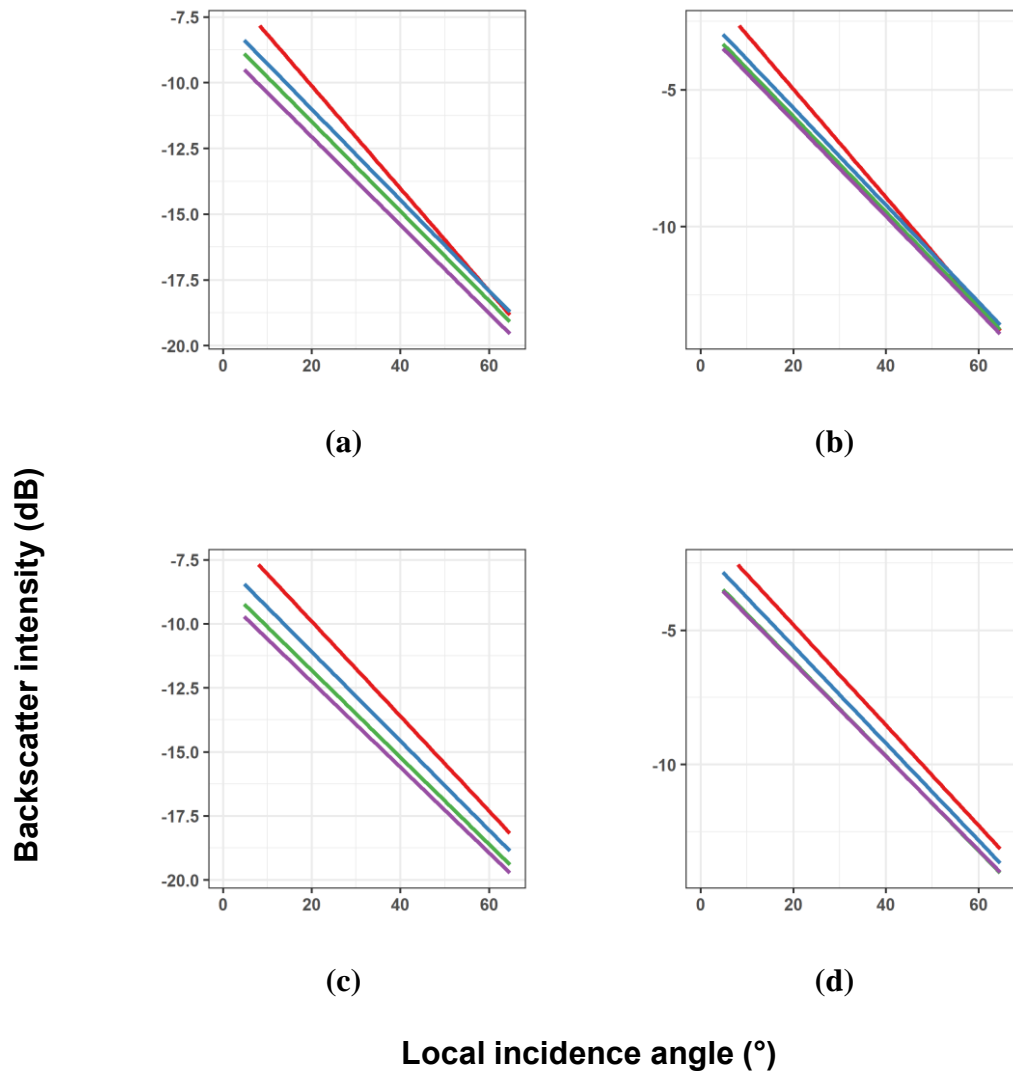


Figure 16: Linear regression relationship between uncorrected backscatter values and LIA in unburnt pixels as a function of the DC class, for **(a)** Sentinel-1A (C-VH); **(b)** Sentinel-1A (C-VV); **(c)** Sentinel-1B (C-VH); **(d)** Sentinel-1B (C-VV). The regression parameters are presented in (Table 4.1).

Table 2: Linear regression between C-VH backscatter values of unburnt pixels and LIA as a function of the sensor, polarization, and DC class. All the regressions are significant at $p < 0.001$. The DC-Class column colours are reflected in plots of (Figure 16).

Sensor & Polarization	DC-Class	Mean backscatter (dB)	Mean DC	Linear Regression Parameters		
				Equation	R ²	N
S1A VV	0 to 1	-13.61	0.58	$y = -6.20 + -0.19(x)$	0.408	83413
	1 to 10	-13.99	3.94	$y = -7.55 + -0.17(x)$	0.331	735476
	10 to 100	-14.45	35.26	$y = -8.07 + -0.17(x)$	0.328	666649
	100 to 1000	-14.98	346.90	$y = -8.70 + -0.17(x)$	0.324	1143507
S1B VV	0 to 1	-13.24	0.61	$y = -6.14 + -0.19(x)$	0.421	35631
	1 to 10	-14.14	4.48	$y = -7.60 + -0.17(x)$	0.344	703635
	10 to 100	-14.77	35.75	$y = -8.41 + -0.17(x)$	0.326	772728
	100 to 1000	-15.16	343.66	$y = -8.91 + -0.17(x)$	0.329	1114588
S1A VH	0 to 1	-8.51	0.58	$y = -0.94 + -0.20(x)$	0.438	83341
	1 to 10	-8.73	3.92	$y = -2.11 + -0.18(x)$	0.366	739908
	10 to 100	-9.02	35.24	$y = -2.48 + -0.17(x)$	0.365	667006
	100 to 1000	-9.17	342.10	$y = -2.65 + -0.17(x)$	0.356	1117419
S1B VH	0 to 1	-8.17	0.61	$y = -0.99 + -0.19(x)$	0.431	35537
	1 to 10	-8.76	4.49	$y = -1.97 + -0.18(x)$	0.377	702264
	10 to 100	-9.23	35.75	$y = -2.63 + -0.18(x)$	0.364	771789
	100 to 1000	-9.24	343.68	$y = -2.70 + -0.17(x)$	0.359	1113898

Following [21], the extracted radar backscatters were normalized for the LIA with the following formula:

$$\bar{\sigma}^{\circ} = \sigma^{\circ}(\text{dB}) - \left(\theta_{\text{inc}} \times \frac{\Delta\sigma^{\circ}}{\Delta\theta_{\text{inc}}} \right) \quad (6)$$

Where:

- $\bar{\sigma}^{\circ}$ is the corrected backscatter for LIA dependence (dB)
- $\sigma^{\circ}(\text{dB})$ is the uncorrected dependent backscatter (dB)
- θ_{inc} is the local incidence angle (LIA) (degree)
- $\Delta\sigma^{\circ}/\Delta\theta_{\text{inc}}$ is the regression slope provided in Table 2 as a function of the sensor, polarization, and DC class.

The resulting corrected backscatters do not show any relationship with LIA (Figure 17). Huang et al. [45] reported the same trend between these two variables but with a different normalization method. Since all the other factors (tree cover and incidence angle) were removed by masking, what is left is the effect of the climate, which is here proxied by the DC classes.

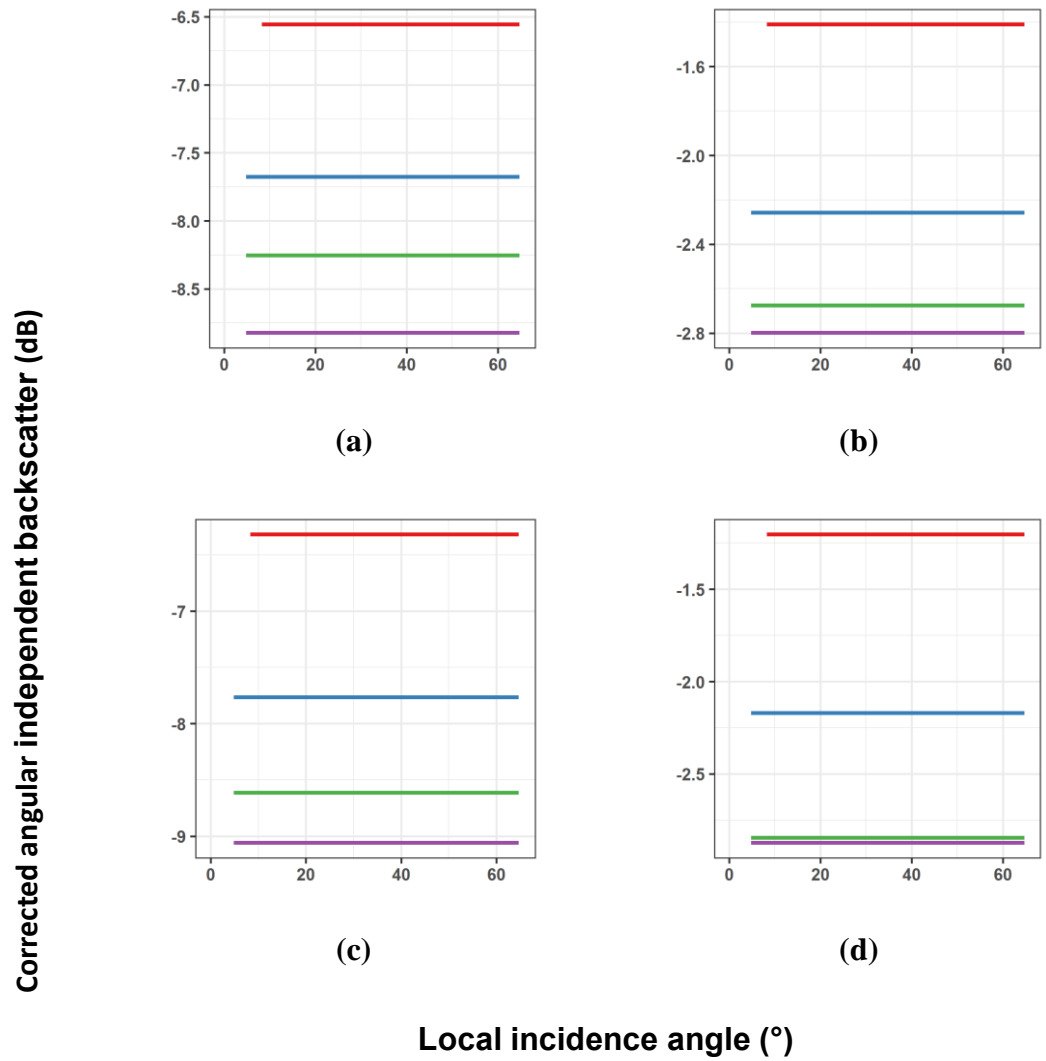


Figure 17: Relationship between the LIA and corrected backscatter values in unburnt pixels with the DC classes, for **(a)** Sentinel-1A (C-VH); **(b)** Sentinel-1A (C-VV); **(c)** Sentinel-1B (C-VH); **(d)** Sentinel-1B (C-VV).

Backscatter values in Figure 18 decreased with DC classes. Further investigations into the DC classes showed that the backscattered intensity was more sensitive to extremely wet soils (DC class = 0.1 to 1) but less sensitive to the transition between dry (DC class = 1 to 10, 10 to 100) and extremely dry (DC class = 100 to 1000) soils. The C-VH shows clearer sensitivity to DC classes in S-1A and S-1B compared to the C-VV. However, the mean backscatter values corresponding to the C-VV are higher than in the C-VH. The S1-B has a lower effect than the S1-A in terms of mean backscatter values. The DC index was created to represent the wetness of the slow-drying deep layers of the soil. DC values above 1 mean that the soils in that situation are dry, and lower values indicate that they are wet. DC values corresponding to dry conditions were only observed in July, August, September, and October 2018 (Table 1).

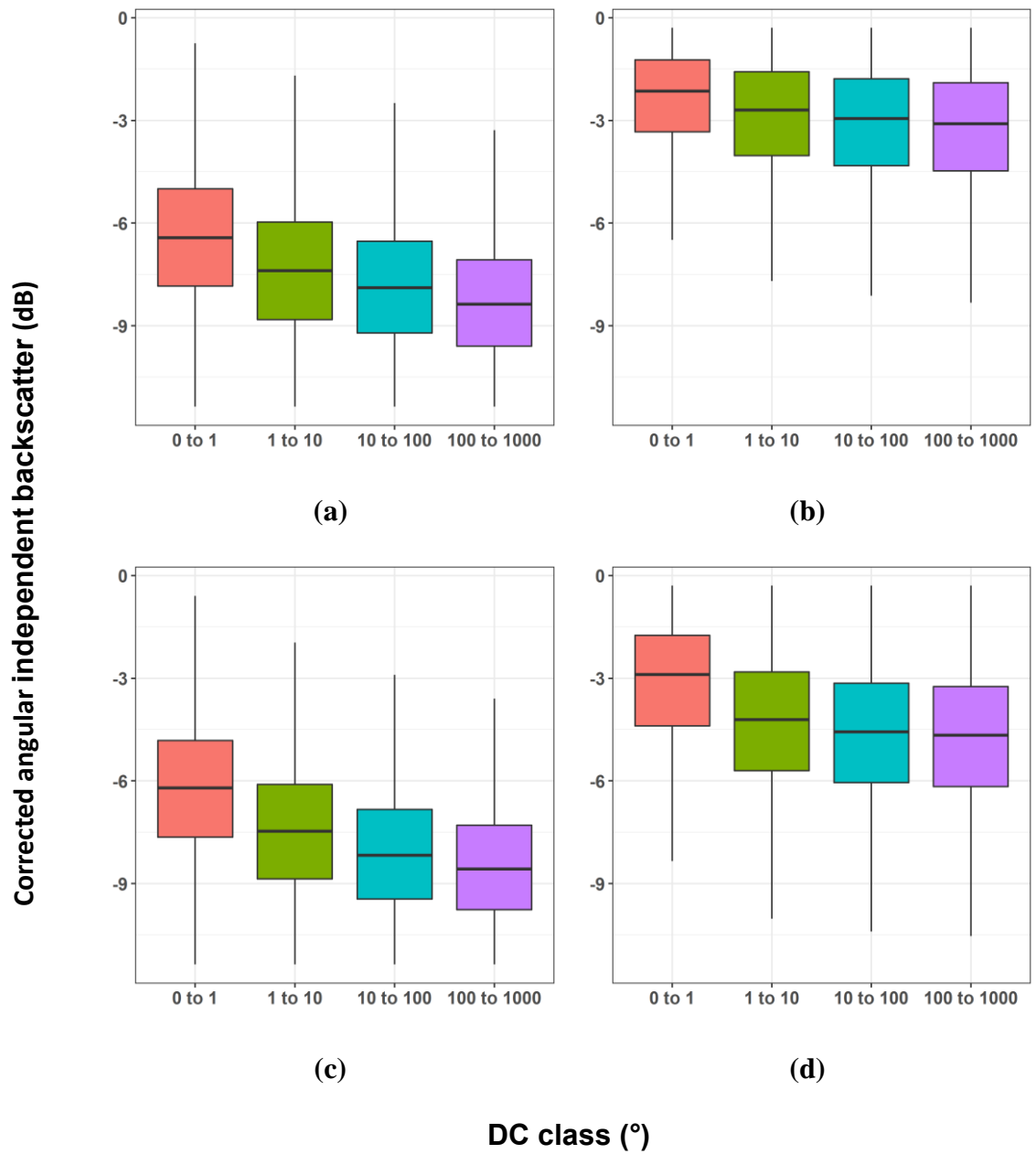


Figure 18: Distribution of corrected backscatter values in unburnt pixels with the DC classes, for (a) Sentinel-1A (C-VH); (b) Sentinel-1A (C-VV); (c) Sentinel-1B (C-VH); (d) Sentinel-1B (C-VV).

4.2 Burnt Areas

The second research question relates to fire's effect on the relationship between corrected backscatter and DC classes. As observed in the pre-fire observation, the relationship between pre-fire normalized backscattered intensity and DC classes is similar (Figure 19). However, with respect to observations in Figure 18 (a-d), the mean backscatter values in Figure 19 (a-d) are less sensitive to DC classes. Such as for the unburnt areas (Figure 18), boxplots in Figure 19 show that C-VH is more able to discriminate between different DC groups with respect to C-VV. The C-VH backscatter difference between DC classes (0 to 1) and (100 to 1000) was +0.9 dB, compared to +0.5 dB in C-VV. Backscatter values from the C-VH showed higher sensitivity than the C-VV in pre-fire SAR observations in a Savannah ecosystem [46]. The higher sensitivity of C-VH to the DC values is likely linked to the fact that the relative scattering strength of C-VH is mainly volume scattering, i.e., vegetation canopy [47 - Table 2.2]. Moreover, in VH biomass backscattering, contributions from the surface and double-bounce scatterers are minimal [48], and therefore high accuracy of volume scattering is expected in the pre-burn datasets. Co-polarized C-VV scattering strength is mainly double bounce and rough surface scattering [47][48].

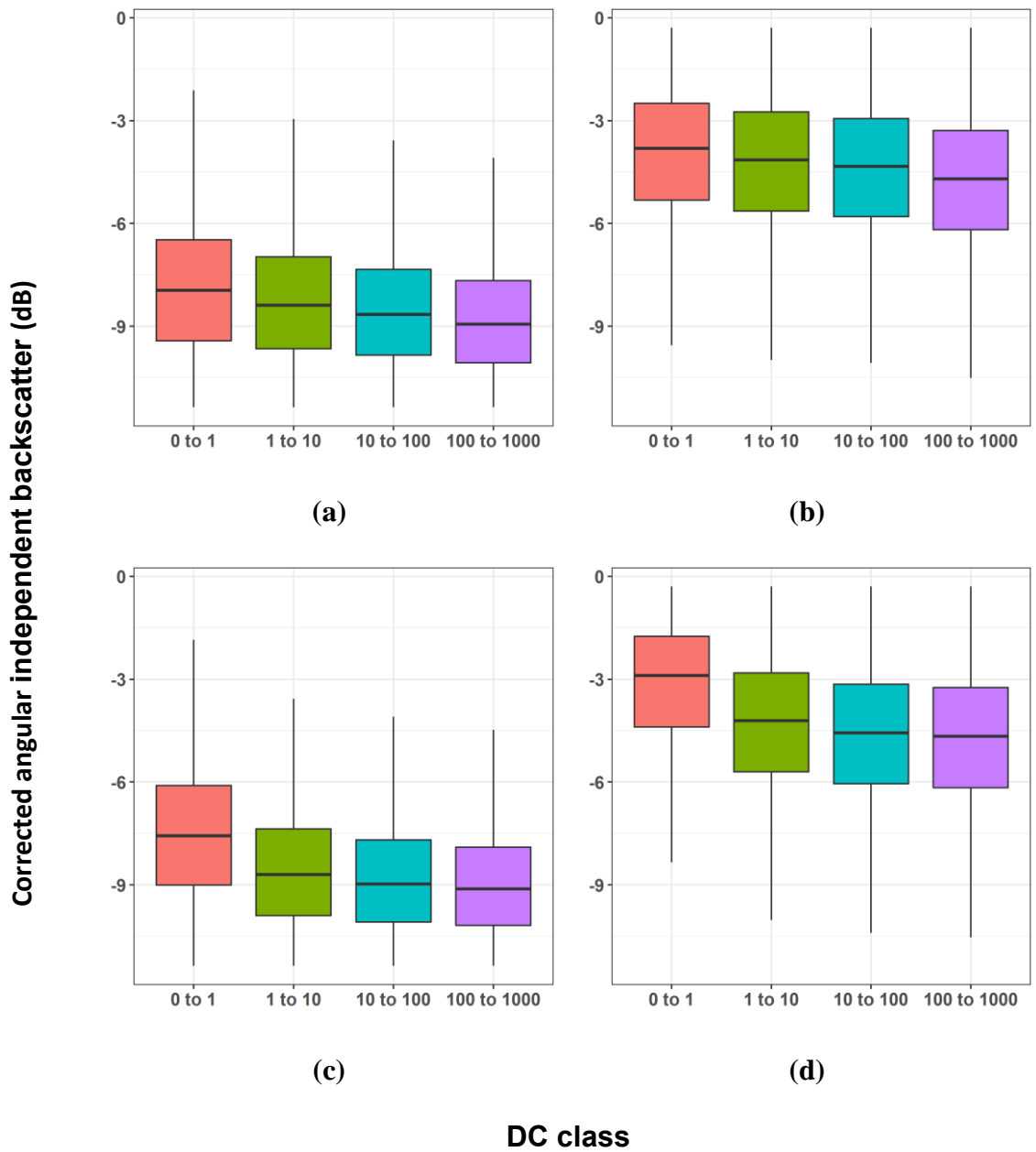


Figure 19: Distribution of corrected backscatter values before fire in fire-affected pixels with the DC classes, for (a) Sentinel-1A (C-VH); (b) Sentinel-1A (C-VV); (c) Sentinel-1B (C-VH); (d) Sentinel-1B (C-VV).

For the post-fire data analysis, the C-VV polarization was not considered because the C-VH polarization provided a clearer change dynamic between the corrected radar backscatter values and the DC classes than the C-VV polarization. To better understand the postfire behaviour of radar backscatters, the postfire period was divided into classes of the number of days after the fire (0 to 30, 30 to 90, 90 to 180, 180 to 360 and 360 to inf). Boxplots corresponding to DC class (0 to 10) are missing for the 0 to 30 and 30 to 90 periods after fire for the S1-B case because of a lack of imagery. Figures 20 and 21 showed no significant change in post-fire C-VH backscatters with DC classes for the period after the fire from zero to 360 days. This trend is dissimilar to what is observed over the unburned sites (Figure 18) and with the pre-fire data (Figure 19). One probable reason for this result is the dielectric property of wood ash that may have influenced post-burn backscatter values, as highlighted in [21]. However, after 360 days, the backscatter-DC relationship became similar to the observations over unburned areas (Figure 18) and with data before the fire (Figure 19). A reasonable hypothesis for the loss of the inverse correlation between C-VH and DC values right after a fire up to 360 days is the decrease of the volume scattering component, i.e., the leaves in the canopy crown. After a fire event, the leaves are charred if not completely burned, thus not contributing to the volume scattering as much as healthy leaves [49][50]. As explained in [51], diverging trends in C-band post-fire backscattering can also be attributed to rainfall, reduced soil moisture and retarded vegetation death.

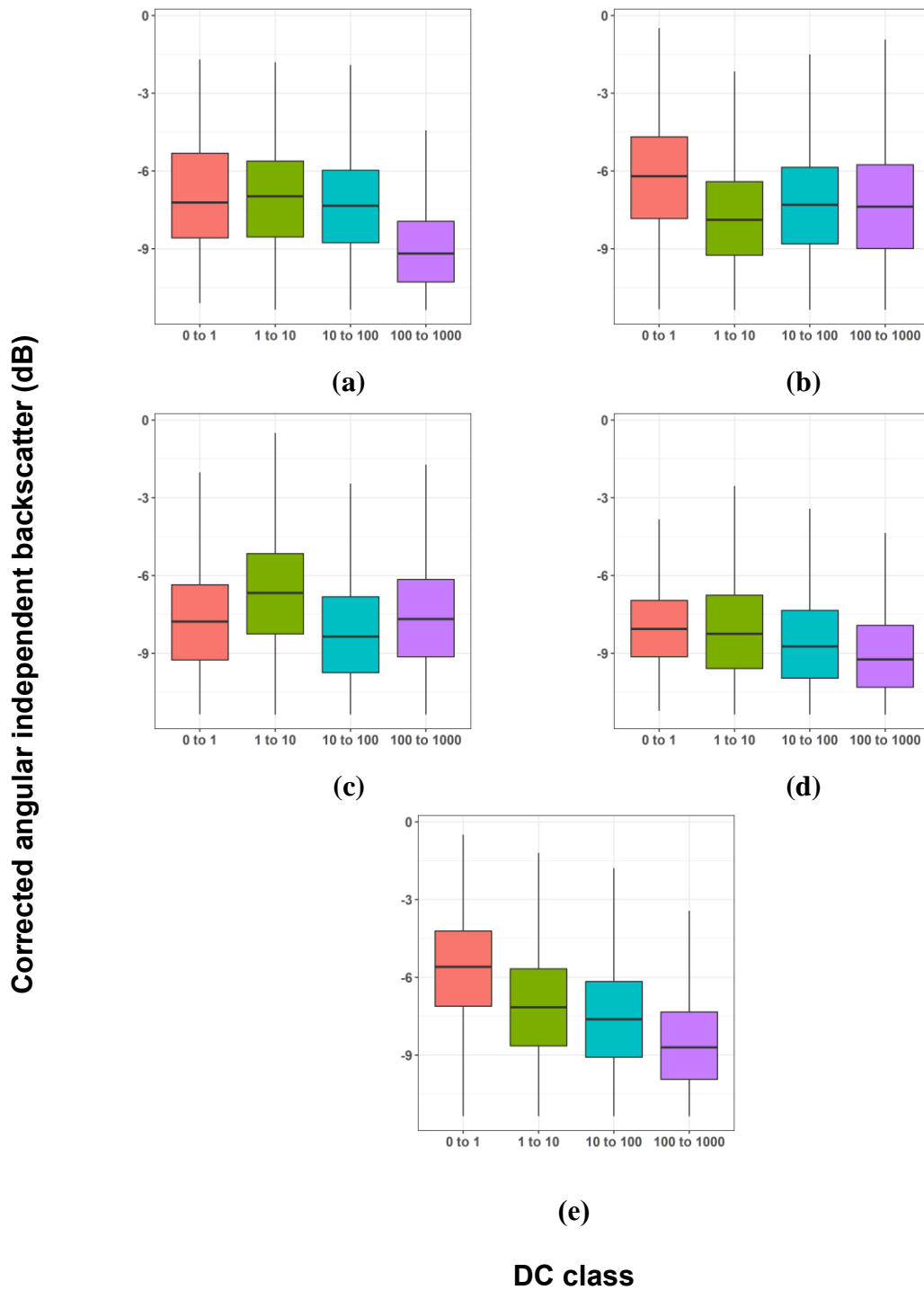
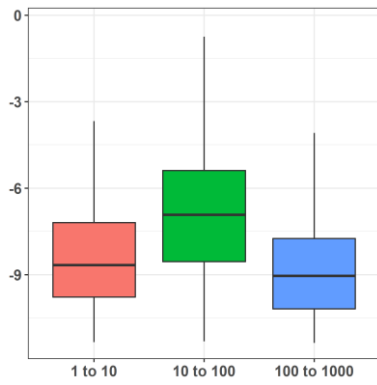
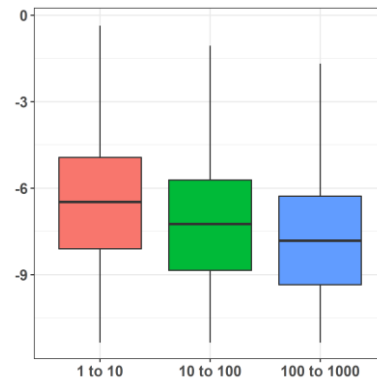


Figure 20: Distribution of corrected Sentinel-1A C-VH backscatter, grouped by DC class for (a) 0 to 30; (b) 30 to 90; (c) 90 to 180; (d) 180 to 360; (e) 360 to inf days after the fire event.

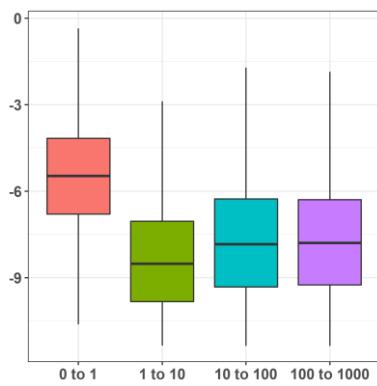
Corrected angular independent backscatter (dB)



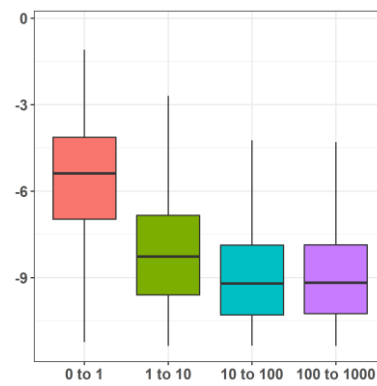
(a)



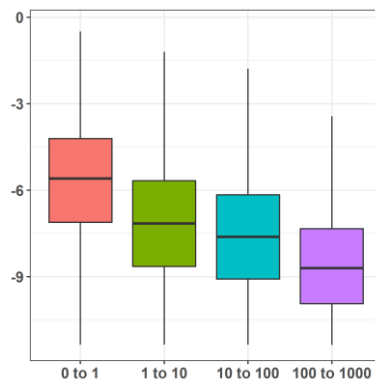
(b)



(c)



(d)



(e)

DC class

Figure 21: Distribution of corrected Sentinel-1B C-VH backscatter, grouped by DC class for (a) 0 to 30; (b) 30 to 90; (c) 90 to 180; (d) 180 to 360; (e) 360 to inf days after the fire event.

After 360 days from the fire event (360 to Inf), the C-VH captured vegetation recovery but was less sensitive in terms of distinction of extremely wet sites, as seen in pre-fire and unburnt observations. For instance, for the S1-B cases, the average corrected backscatter corresponding to the 360 to Inf period (Figure 21e) was -7.5 dB, compared to -5 dB for the pre-fire observations in (Figure 19c). As already shown by [52], C-band backscatters used for monitoring post-fire vegetation recovery are influenced by several factors. In particular, post-fire C-band backscatters never returned to the pre-fire levels due to the disturbance of the vegetation structure and density with the fire. Since the C-VH is sensitive to vegetation structure, the C-VH backscatter also depends on the post-burn regeneration rate. By contrast, [53] reported that the L-band performed better than the C-band in change detection of post-fire vegetation structure in a Mediterranean environment. Therefore, it is preferable to use a combination of L and C bands [53][54]. An even better method is the synergistic use of radar and optical images, given that they give different information over the surveyed area [55].

5. Conclusions

Time series 10 m Sentinel-1 C-VV and C-VH images, acquired from January 2018 to December 2020, were used to analyze the correlation between backscatter and soil wetness estimated using DC values as a proxy. The study was carried out over 502.42 km² in North-western Portugal. C-VH radar backscatters were found to be better related to the DC values than C-VV radar backscatters. Low DC values, i.e., less than or equal to 1, have a median C-VH backscatter about 2 dB higher with respect to DC values above 10. As observed in the unburnt sites, the relationship between backscatter and DC was monitored in the sites affected by fire events (Figure 4) over the 181-day satellite coverage. Results show that the C-VH backscatters are not sensitive to changes in DC values right after a fire event. Similar to the trend in pre-fire and unburnt sites, the relationship between these variables becomes similar after at least 360 days of the fire date.

The study was done in a Mediterranean region of North-western Portugal with specific tree species, and it is necessary to have this analysis done over other Mediterranean regions with other tree species. In addition, bilinear interpolation was used to assign DC values to the fire maps, as the sourced FWI-related weather records have low spatial resolutions. Therefore, high-resolution DC data should ensure that spatially-derived DC values represent fine-scale soil moisture conditions.

References

- [1] Pinto, M. M., DaCamara, C. C., Trigo, I. F., Trigo, R. M., & Turkman, K. F. (2018). Fire danger rating over Mediterranean Europe based on fire radiative power derived from Meteosat. *Natural Hazards and Earth System Sciences*, 18(2), 515–529. <https://doi.org/10.5194/nhess-18-515-2018>
- [2] Pyne, S. J. (2009). Eternal Flame: An Introduction to the Fire History of the Mediterranean. In *Earth Observation of Wildland Fires in Mediterranean Ecosystems* (pp. 11–26). Springer Berlin Heidelberg. https://doi.org/10.1007/978-3-642-01754-4_2
- [3] Gonçalves, A. C., & Sousa, A. M. O. (2017). The Fire in the Mediterranean Region: A Case Study of Forest Fires in Portugal. *Mediterranean Identities - Environment, Society, Culture*. InTech. Pp 311. <https://doi.org/10.5772/intechopen.69410>
- [4] Van Wagner, C. (1987). Development and Structure of the Canadian Forest Fire Weather Index System. Canada, Government of Canada, Canadian Forestry Service, National Forestry Institute. Forestry Technical Report N°35, Petawawa (Canada), pp 13
- [5] Stocks, B., Lawson, B., Alexander, M., Van Wagner, C., McAlpine, R., Lynham, T., & Dubé D. (1989). Canadian Forest Fire Danger Rating System: An Overview. *The Forestry Chronicle* 65(4), 258-265. <https://doi.org/10.5558/tfc65258-4>
- [6] Oldford, S., Leblon, B., Maclean, D., & Flannigan, M. (2006). Predicting slow-drying fire weather index fuel moisture codes with NOAA-AVHRR images in Canada's northern boreal forests. *International Journal of Remote Sensing*, 27(18), 3881–3902. <https://doi.org/10.1080/01431160600784234>
- [7] European Centre for Medium-Range Weather Forecasts (2022). Describing ECMWF's forecasts and forecasting system. Retrieved January 2022 from: <https://www.ecmwf.int/sites/default/files/elibrary/2012/17412-describing-ecmwfs-forecasts-and-forecasting-system.pdf>

- [8] Wotton, B. M. (2009). Interpreting and using outputs from the Canadian Forest Fire Danger Rating System in research applications. *Environmental and Ecological Statistics*, 16(2), 107–131. <https://doi.org/10.1007/s10651-007-0084-2>
- [9] Leblon, B. (2005). Monitoring Forest Fire Danger with Remote Sensing. *Natural Hazards*, 35(3), 343–359. <https://doi.org/10.1007/s11069-004-1796-3>
- [10] Rostami, A., Shah-Hosseini, R., Asgari, S., Zarei, A., Aghdami-Nia, M., & Homayouni, S. (2022). Active Fire Detection from Landsat-8 Imagery Using Deep Multiple Kernel Learning. *Remote Sensing*, 14(4), 992. <https://doi.org/10.3390/rs14040992>
- [11] Vetrita, Y., Prasasti, I., Haryani, N. S., Priyatna, M., & Rokhis Khomarudin, M. (2012). Drought and Fine Fuel Moisture Code Evaluation: An Early Warning System for Forest/Land Fire using Remote Sensing Approach. *International Journal of Remote Sensing and Earth Sciences*, 9(2), 140-147 <http://dx.doi.org/10.30536/j.ijreses.2012.v9.a1841>
- [12] Lee, J.-S., & Pottier, E. (2009). *Polarimetric Radar Imaging: From Basics to Applications (Optical Science and Engineering)*. CRC Press. Pp 5-6. <https://doi.org/10.1201/9781420054989>
- [13] Ruiz-Ramos, J., Marino, A., & Boardman, C. P. (2018). Using Sentinel 1-SAR for monitoring long-term variation in burnt forest areas. *International Geoscience and Remote Sensing Symposium (IGARSS)*, 2018-July, 4901–4904. <https://doi.org/10.1109/IGARSS.2018.8518960>
- [14] Çolak, E., & Sunar, F. (2020). Evaluation of forest fire risk in the Mediterranean Turkish forests: A case study of Menderes region, Izmir. *International Journal of Disaster Risk Reduction*, 45(5), 101479. <https://doi.org/10.1016/j.ijdrr.2020.101479>
- [15] Mitsopoulos, I., Chrysafi, I., Bountis, D., & Mallinis, G. (2019). Assessment of factors driving high fire severity potential and classification in a Mediterranean pine ecosystem. *Journal of Environmental Management*, 235(April), 266-275. <https://doi.org/10.1016/j.jenvman.2019.01.056>

- [16] National Wildfire Coordinating Group (2021). CFFDRS System Overview. Retrieved September 2021 from:
<https://www.nwcg.gov/publications/pms437/cffdrs/overview>
- [17] Leblon, B., Kasischke, E., Alexander, M., Doyle, M., & Abbott, M. (2002). Fire Danger Monitoring Using ERS-1 SAR Images in the Case of Northern Boreal Forests. *Natural Hazards*, 27(3), 231-255.
<https://doi.org/10.1023/A:1020375721520>
- [18] Yang, G., & Di, X. (2011). Adaptation of Canadian Forest Fire Weather Index system and its application. 2011 IEEE International Conference on Computer Science and Automation Engineering. Pp 55-58.
<https://doi.org/10.1109/CSAE.2011.5952422>
- [19] Dimitrakopoulos, A. P., Bemmerzouk, A. M., & Mitsopoulos, I. D. (2011). Evaluation of the Canadian fire weather index system in an eastern Mediterranean environment. *Meteorological Applications*, 18(1), 83–93.
<https://doi.org/10.1002/met.214>
- [20] Bourgeau-Chavez, L. L., Leblon, B., Charbonneau, F., & Buckley, J. R. (2013). Assessment of polarimetric SAR data for discrimination between wet versus dry soil moisture conditions. *International Journal of Remote Sensing* 34(16), 5709-5730. <https://doi.org/10.1080/01431161.2013.796096>
- [21] Abbott, K. N., Leblon, B., Staples, G. C., Maclean, D. A., & Alexander, M. E. (2007). Fire danger monitoring using RADARSAT-1 over northern boreal forests. *International Journal of Remote Sensing*, 28(6), 1317–1338.
<https://doi.org/10.1080/01431160600904956>
- [22] Bourgeau-Chavez, L. L., Riordan, K., & Garwood, G. (2008). Monitoring Fuel Moisture and Improving the Prediction of Wildfire Potential in Boreal Alaska with Satellite C-Band Imaging Radar. *Proceedings of the 2008 IEEE International Geoscience and Remote Sensing Symposium*, Boston, pp. 864-866.
<https://doi.org/10.1109/IGARSS.2008.4779486>

- [23] Leblon, B., Bourgeau-Chavez, L., & San-Miguel-Ayanz, J. (2012). Use of Remote Sensing in Wildfire Management. In Sustainable Development - Authoritative and Leading Edge Content for Environmental Management. InTech. Pp 63. <https://doi.org/10.5772/45829>
- [24] Torres, R., Snoeij, P., Geudtner, D., Bibby, D., Davidson, M., Attema, E., Potin, P., Rommen, B., Floury, N., Brown, M., Traver, I. N., Deghaye, P., Duesmann, B., Rosich, B., Miranda, N., Bruno, C., L'Abbate, M., Croci, R., Pietropaolo, A., & Rostan, F. (2012). GMES Sentinel-1 mission. Remote Sensing of Environment, 120(5), 9–24. <https://doi.org/10.1016/j.rse.2011.05.028>
- [25] Soudani, K., Delpierre, N., Berveiller, D., Hmimina, G., Vincent, G., Morfin, A., & Dufrêne, É. (2021). Potential of C-band Synthetic Aperture Radar Sentinel-1 time-series for the monitoring of phenological cycles in a deciduous forest. International Journal of Applied Earth Observation and Geoinformation, 104(12), 102505. <https://doi.org/10.1016/j.jag.2021.102505>
- [26] Sutariya, S., Hirapara, A., Meherbanali, M., Tiwari, M. k., Singh, V., & Kalubarme, M. (2021). Soil Moisture Estimation using Sentinel-1 SAR Data and Land Surface Temperature in Panchmahal District, Gujarat State. International Journal of Environment and Geoinformatics, 8(1), 65-77. <https://doi.org/10.30897/ijegeo.777434>
- [27] Wang, L., Quan, X., He, B., Yebra, M., Xing, M., & Liu, X. (2019). Assessment of the Dual Polarimetric Sentinel-1A Data for Forest Fuel Moisture Content Estimation. Remote Sensing, 11(13), 1568. <https://doi.org/10.3390/rs11131568>
- [28] Institute for the Conservation of Nature and Forestry of Portugal (2014). The Portuguese National Forest Inventory. University of Lisbon. May 19, 2014. Retrieved January 2022 from: http://ecofun.fc.ul.pt/Activities/Desertification2014/docs2/SousaUva_The%20Portuguese%20National%20Forest%20Inventory.pdf

- [29] Kottek, M., Grieser, J., Beck, C., Rudolf, B., & Rubel, F. (2006). World Map of the Köppen-Geiger climate classification updated. 15(3), 259–263.
<https://doi.org/10.1127/0941-2948/2006/0130>
- [30] Portuguese Institute of the Sea and the Atmosphere (2022). Mean, maximum, and minimum monthly temperature and total precipitation in 1981-2010. Retrieved January 2022 from: <http://ipma.pt/pt/oclima/normais.clima/1981-2010/normalclimate8110.jsp>
- [31] Pereira, M. G., Trigo, R. M., da Camara, C. C., Pereira, J. M. C., & Leite, S. M. (2005). Synoptic patterns associated with large summer forest fires in Portugal. *Agricultural and Forest Meteorology*, 129(1–2), 11–25.
<https://doi.org/10.1016/j.agrformet.2004.12.007>
- [32] San-Miguel-Ayanz, J., Durrant, T., Boca, R., Maianti, P., Libertá, G., Artes Vivancos, T., Jacome Felix Oom, D., Branco, A., De Rigo, D., Ferrari, D., Pfeiffer, H., Grecchi, R., Nuijten, D., Onida, M. & Loffler, P., (2021). Forest Fires in Europe, Middle East and North Africa 2020. Publications Office of the European Union, Luxembourg, 2021. pp 70. <https://doi:10.2760/059331>
- [33] Paulo B., Giuseppe A., Roberto B., Andrea C., Jan K., Giorgio L., Jesus San-Miguel-Ayanz J., Guido S., Ernst S., & Hans-Helmut Dierks (2007). Forest Fires in Europe 2006. Publications Office of the European Union, Luxembourg, 2007. pp 25.
- [34] San-Miguel-Ayanz, J., Durrant, T., Boca, R., Maianti, P., Libertá, G., Artés-Vivancos, T., Oom, D., Branco, A., de Rigo, D., Ferrari, D., Pfeiffer, H., Grecchi, R., & Nuijten, D. (2022). Advance Report on Forest Fires in Europe, Middle East and North Africa 2021. Publications Office of the European Union, Luxembourg, 2022. pp 4. <https://doi.org/10.2760/039729>
- [35] Enes, T., Lousada, J., Aranha, J., Cerveira, A., Alegria, C., & Fonseca, T. (2019). Size-density trajectory in regenerated maritime pine stands after fire. *Forests*, 10(12). 1057. <https://doi.org/10.3390/f10121057>

- [36] Hansen, M. C., Potapov, P. v., Moore, R., Hancher, M., Turubanova, S. A., Tyukavina, A., Thau, D., Stehman, S. v., Goetz, S. J., Loveland, T. R., Kommareddy, A., Egorov, A., Chini, L., Justice, C. O., & Townshend, J. R. G. (2013). High-Resolution Global Maps of 21st-Century Tree cover Change. *Science*, 342(6160), 850–853. <https://doi.org/10.1126/science.1244693>
- [37] Ciobotaru, A. M., Patel, N., & Pintilii, R. D. (2021). Tree cover loss in the Mediterranean region—an increasingly serious environmental issue. *Forests*, 12(10), 1341. <https://doi.org/10.3390/f12101341>
- [38] Di Giuseppe, F., Vitolo, C., Krzeminski, C., Barnard, C., Maciel, C., San-Miguel-Ayanz, J. (2020). Fire Weather Index: the skill provided by the European Centre for Medium-Range Weather Forecasts ensemble prediction. *Natural Hazards and Earth System Sciences*, 20(8), 2365-2378. <https://doi.org/10.5194/nhess-20-2365-2020>
- [39] Turner, J.A. (1972). The Drought Code Component of the Canadian Forest Fire Behaviour System. Environment Canada, Canadian Forestry Service, Headquarters, Ottawa. Publication Number 1316. pp 5.
- [40] European Centre for Medium-Range Weather Forecasts (2021). Fire Danger Forecast. Retrieved February 2022 from: <https://effis.jrc.ec.europa.eu/about-effis/technical-background/fire-danger-forecast>
- [41] Kaplan, G., Fine, L., Lukyanov, V., Manivasagam, V. S., Tanny, J., & Rozenstein, O. (2021). Normalizing the local incidence angle in sentinel-1 imagery to improve leaf area index, vegetation height, and crop coefficient estimations. *Land*, 10(7), 680. <https://doi.org/10.3390/land10070680>
- [42] O'Grady, D., Leblanc, M., & Gillieson, D. (2013). Relationship of local incidence angle with satellite radar backscatter for different surface conditions. *International Journal of Applied Earth Observation and Geoinformation* 24(10), 42-53. <https://doi.org/10.1016/j.jag.2013.02.005>
- [43] Vollrath, A., Mullissa, A., & Reiche, J. (2020). Angular-based radiometric slope correction for Sentinel-1 on Google Earth Engine. *Remote Sensing*, 12(11), 1867. <https://doi.org/10.3390/rs12111867>

- [44] Paluba, D., Laštovička, J., Mouratidis, A., & Štych, P. (2021). Land cover-specific local incidence angle correction: A method for time-series analysis of forest ecosystems. *Remote Sensing*, 13(9), 1743. <https://doi.org/10.3390/rs13091743>
- [45] Huang, W., Sun, G., Ni, W., Zhang, Z., & Dubayah, R. (2015). Sensitivity of multi-source SAR backscatter to changes in forest aboveground biomass. *Remote Sensing*, 7(8), 9587–9609. <https://doi.org/10.3390/rs70809587>
- [46] Mathieu, R., Main, R., Roy, D.P., Naidoo, L., & Yang, H. (2019). The Effect of Surface Fire in Savannah Systems in the Kruger National Park (KNP), South Africa, on the Backscatter of C-Band Sentinel-1 Images. *Fire*, 2(3).37. <https://doi.org/10.3390/fire2030037>
- [47] Kellndorfer, J. (2019). Using SAR Data for Mapping Deforestation and Forest Degradation. In: Flores-Anderson, A.I., Herndon, K.E., Thapa, R.B., Cherrington, E. (Eds.), *The SAR Handbook: Comprehensive Methodologies for Forest Monitoring and Biomass Estimation*. pp 68. <https://doi:10.25966/nr2c-s697>
- [48] Meyer, F. (2019). Spaceborne Synthetic Aperture Radar: Principles, Data Access, and Basic Processing Techniques. In: Flores-Anderson, A.I., Herndon, K.E., Thapa, R.B., Cherrington, E. (Eds.), *The SAR Handbook: Comprehensive Methodologies for Forest Monitoring and Biomass Estimation*. pp 28. <https://doi:10.25966/ez4f-mg98>
- [49] Imperatore, P., Azar, R., Calo, F., Stroppiana, D., Brivio, P. A., Lanari, R., & Pepe, A. (2017). Effect of the Vegetation Fire on Backscattering: An Investigation Based on Sentinel-1 Observations. *IEEE Journal of Selected Topics in Applied Earth Observations and Remote Sensing*, 10(10), 4478–4492. <https://doi.org/10.1109/JSTARS.2017.2717039>
- [50] Tanase, M. A., Santoro, M., de La Riva, J., Pérez-Cabello, F., & le Toan, T. (2010). Sensitivity of X-, C-, and L-Band SAR Backscatter to Burn Severity in Mediterranean Pine Forests. *IEEE Transaction. on Geoscience. and Remote Sensing*, 48(10), 3663. <https://doi.org/10.1109/TGRS.2010.2049653>

- [51] Belenguer-Plomer, M., Chuvieco, E., Tanase, M. (2019). Temporal Decorrelation of C-Band Backscatter Coefficient in Mediterranean Burned Areas. *Remote Sensing*, 11(22), 2661. <https://doi:10.3390/rs11222661>
- [52] Zhou, Z., Liu, L., Jiang, L., Feng, W., & Samsonov, S. V. (2019). Using long-term SAR backscatter data to monitor post-fire vegetation recovery in tundra environment. *Remote Sensing*, 11(19), 2230. <https://doi.org/10.3390/rs11192230>
- [53] Tanase, M., de la Riva, J., Santoro, M., Pérez-Cabello, F., & Kasischke, E. (2011). Sensitivity of SAR data to post-fire forest regrowth in Mediterranean and boreal forests. *Remote Sensing of Environment*, 115(8), 2075–2085. <https://doi.org/10.1016/j.rse.2011.04.009>
- [54] Tanase, M. A., Santoro, M., Aponte, C., & de la Riva, J. (2014). Polarimetric Properties of Burned Forest Areas at C- and L-Band. *IEEE Journal of Selected Topics in Applied Earth Observations and Remote Sensing*, 7(1), 267–276. <https://doi.org/10.1109/JSTARS.2013.2261053>
- [55] Bernhard, E.-M., Stein, E., Twele, A., & Gähler, M. (2012). Synergistic use of optical and radar data for rapid mapping of forest fires in the European Mediterranean. *The International Archives of the Photogrammetry, Remote Sensing and Spatial Information Sciences*, XXXVIII-4/W19, 27–32. <https://doi.org/10.5194/isprsarchives-XXXVIII-4-W19-27-2011>

Appendix: Regression Equation

Table A.1.1: Linear Regression between post-fire corrected C-VH backscatter values and the DC classes for a) Sentinel-1 A and b) Sentinel-1 B, as a function of the number of days after the fire. All the regressions are significant at $p < 0.001$

Sensor	DC-Class	Days after fire	Mean DC	Equation	R ²	N
S1A	0 to 1	0 to 30	0.72	$y = -7.95 + -0.13(x)$	0.267	942
		30 to 90	0.83	$y = -6.72 + -0.19(x)$	0.262	3618
		90 to 180	0.76	$y = -8.65 + -0.18(x)$	0.326	4717
		180 to 3650	0.87	$y = -6.21 + -0.20(x)$	0.542	4317
	1 to 10	0 to 30	4.73	$y = -7.19 + -0.19(x)$	0.413	4034
		30 to 90	3.10	$y = -8.17 + -0.18(x)$	0.302	37754
		90 to 180	3.90	$y = -7.05 + -0.21(x)$	0.368	66786
		180 to 3650	3.67	$y = -8.14 + -0.18(x)$	0.346	176998
	10 to 100	0 to 30	32.55	$y = -7.46 + -0.19(x)$	0.420	6481
		30 to 90	33.45	$y = -7.76 + -0.19(x)$	0.376	38187
		90 to 180	28.13	$y = -10.13 + -0.18(x)$	0.202	49140
		180 to 3650	36.82	$y = -9.10 + -0.17(x)$	0.311	167553
	100 to 1000	0 to 30	490.02	$y = -10.83 + -0.15(x)$	0.201	56487
		30 to 90	327.01	$y = -8.04 + -0.20(x)$	0.314	45745
		90 to 180	340.85	$y = -8.15 + -0.20(x)$	0.426	32524
		180 to 3650	342.42	$y = -10.08 + -0.16(x)$	0.291	372817

S1B	0 to 1	90 to 180	0.74	$y = -5.48 + -0.20(x)$	0.355	6246
		180 to 3650	0.69	$y = -6.19 + -0.19(x)$	0.478	7337
	1 to 10	0 to 30	4.16	$y = -8.84 + -0.15(x)$	0.292	3522
		30 to 90	3.92	$y = -6.68 + -0.21(x)$	0.372	32609
		90 to 180	5.83	$y = -9.41 + -0.16(x)$	0.260	60294
		180 to 3650	5.18	$y = -8.43 + -0.18(x)$	0.345	165025
	10 to 100	0 to 30	29.04	$y = -7.40 + -0.20(x)$	0.425	8432
		30 to 90	37.68	$y = -7.98 + -0.20(x)$	0.345	42850
		90 to 180	29.35	$y = -8.88 + -0.20(x)$	0.284	59616
		180 to 3650	39.01	$y = -9.96 + -0.16(x)$	0.277	183932
	100 to 1000	0 to 30	493.42	$y = -10.40 + -0.16(x)$	0.236	46226
		30 to 90	324.21	$y = -8.64 + -0.19(x)$	0.313	49973
		90 to 180	335.58	$y = -8.43 + -0.19(x)$	0.415	32171
		180 to 3650	338.96	$y = -9.89 + -0.16(x)$	0.315	360085

Table A.1.2: Linear Regression between pre-fire corrected backscatter values and the DC classes as a function of the polarization, sensor and DC class. All the regressions are significant at $p < 0.001$

Sensor	Polarization	DC-Class	Mean backscatter (dB)	Mean DC	Linear Regression		
					Equation	R ²	N
S1A	VH	0 to 1	-14.29	0.71	$y = -8.48 + -0.16(x)$	0.320	37356
		1 to 10	-14.44	3.97	$y = -8.88 + -0.16(x)$	0.275	317634
		10 to 100	-14.81	40.44	$y = -9.27 + -0.16(x)$	0.288	340486
		100 to 1000	-15.19	346.99	$y = -9.75 + -0.16(x)$	0.273	506737
	VV	0 to 1	-9.50	0.71	$y = -3.76 + -0.16(x)$	0.334	37061
		1 to 10	-9.43	3.87	$y = -3.97 + -0.15(x)$	0.282	339411
		10 to 100	-9.52	40.32	$y = -4.33 + -0.15(x)$	0.283	342235
		100 to 1000	-9.78	346.43	$y = -4.70 + -0.15(x)$	0.271	504283
S1B	VH	0 to 1	-13.87	0.80	$y = -7.99 + -0.16(x)$	0.336	16164
		1 to 10	-14.74	4.84	$y = -9.30 + -0.15(x)$	0.286	318379
		10 to 100	-15.27	40.61	$y = -9.75 + -0.16(x)$	0.290	359222
		100 to 1000	-15.43	346.71	$y = -9.97 + -0.16(x)$	0.286	518278
	VV	0 to 1	-8.98	0.79	$y = -2.61 + -0.18(x)$	0.355	16007
		1 to 10	-9.50	4.84	$y = -4.05 + -0.15(x)$	0.291	317553
		10 to 100	-9.86	40.60	$y = -4.56 + -0.15(x)$	0.286	358454
		100 to 1000	-9.88	346.78	$y = -4.69 + -0.15(x)$	0.277	517317

Curriculum Vitae

Candidate's full name: Adedipe, Opeyemi Emmanuel

Universities attended (with dates and degrees obtained):

- Ongoing: Master of Forestry in Forestry and Environmental Management, University of New Brunswick, Fredericton, Canada.
- Ongoing: Master of Science in Forest Science, University of Padova, Padua, Italy.
- 2014-2018: Bachelor of Agricultural Technology in Crop, Soil and Pest Management, Federal University of Technology, Akure.

Publications: None

Conference Presentations: None